The Biomechanics of Mammary Epithelial Morphogenesis

by

Matthew Perrone

A thesis
presented to the University of Waterloo
in fulfillment of the
thesis requirement for the degree of
Master of Applied Science
in
Civil Engineering

Waterloo, Ontario, Canada, 2017

Author's Declaration

This thesis consists of material all of which I authored or co-authored: see Statement of Contributions included in the thesis. This is a true copy of the thesis, including any required final revisions, as accepted by my examiners.

I understand that my thesis may be made electronically available to the public.

Statement of Contributions

Chapters 2, 3, 5, and 6 of this thesis consist of work paraphrased from a paper that has been submitted for publication. The paper is co-authored by Neil M. Neumann (MD/PhD candidate, Johns Hopkins University), myself, Jim H. Veldhuis (research technician, University of Waterloo), Huiwang Zhan (PhD candidate, Johns Hopkins University), Dr. Peter N. Devreotes (Professor, Johns Hopkins University), Dr. G. Wayne Brodland (Professor, University of Waterloo), and Dr. Andrew J. Ewald (Associate Professor, Johns Hopkins University). Conceptualization: AJE & GWB; investigation: NMN, MP, JHV; formal analysis and visualization: NMN, MP, JHV; provision of reagents: HZ; writing – original draft: NMN, MP, AJE; experimental work: NMN, AJE; computational work: MP, JHV, GWB; writing – review & editing: NMN, MP, JHV, HZ, PND, GWB, AJE; funding and supervision: GWB, PND, AJE.

Chapter 2 consists of work paraphrased from a 2014 paper that was co-authored by Dr. G. Wayne Brodland (Professor, University of Waterloo), Jim H. Veldhuis (research technician, University of Waterloo), Steven Kim (MASc candidate, University of Waterloo), myself, David Mashburn (PhD candidate, Vanderbilt University), and Dr. M. Shane Hutson (Professor, Vanderbilt University). Conceived and designed the experiments: GWB & MSH; performed the experiments: JHV & DM; analyzed the data: SK, MP, JHV, DM, GWB; contributed reagents/materials/analysis tools: JHV & DM; wrote the paper: GWB & MSH; funding and supervision: GWB & MSH.

Chapters 3, 5, and 6 consist of work paraphrased from a 2015 paper that was co-authored by myself, Jim H. Veldhuis (research technician, University of

Waterloo), and Dr. G. Wayne Brodland (Professor, University of Waterloo). Conceptualization: JHV & GWB; investigation, formal analysis, and visualization: MP & JHV; writing – original draft: MP & GWB; writing – review & editing: MP, JHV, GWB; funding and supervision: GWB.

Abstract

Major organs and tissues such as the lung, kidney, liver, and the salivary and mammary glands are complex structures, but share a fundamental building block – epithelial cells. During tissue formation – a process known as morphogenesis – epithelial cells express motile behaviour. Although numerous identified transcripts, genes, and molecular pathways are responsible for the epithelial spatial organization of these organs; the way in which epithelial cells move and rearrange to form tissues is incompletely understood. Advanced imaging techniques provide snapshots of epithelial morphogenesis, but do not reveal cell motions or the forces that drive them. The goal of this study was to use biomechanics and computational modeling to fill this knowledge gap by identifying and confirming the cellular mechanics of mammary epithelial tube morphogenesis. Identifying these motile behaviours connects the transcripts, genes, and molecular pathways responsible for morphogenesis to the resulting cellular movements. In addition, many invasive carcinomas originate in epithelial tissues of major organs and it is the epithelial cells that become malignant. Knowledge of how carcinomas acquire motile behaviours is of particular interest in the field of medicine as it may lead to a better understanding of metastasis – a deadly disease responsible for approximately 90% of cancer-related deaths. Identifying the motile behaviours of epithelial cells during morphogenesis provides a mechanical basis of understanding how invasive carcinomas may move during the early stages of metastasis.

In this study, inference techniques were applied to 3D images of *in vitro* cells in organoids to determine the interfacial tensions associated with the molecular activities and cellular behaviours proposed to drive epithelial tube

morphogenesis. Then, finite element (FE) modeling was used to confirm the sufficiency of the identified interfacial tensions to drive epithelial tube morphogenesis. The model showed that various combinations of interfacial tensions are sufficient to drive cell migration and intercalation and, when combined with a time-varying boundary capture mechanism and high basal stress, are sufficient to drive tube elongation and polarization. Finally, a prediction model was proposed in which cell motility behaviour may be predicted solely by force inference from cell geometry. This study demonstrates that computational modeling can act as a novel window into a biological system by providing insights that cannot be obtained by advanced imaging and other means. This study also illustrates the importance of iterative dialogue between physical experimentation and modelling for developing a quantitative understanding of how cells collectively behave to form complex tissues and organs.

Acknowledgements

I thank my supervisor Dr. G. Wayne Brodland for his support, for teaching me that engineering is an “iterative process”, and for encouraging me to “turn-over as many rocks” as I did during my MASc program.

I also thank Jim H. Veldhuis for his support, for introducing me to the sport of squash, and for being an exceptional travel companion for academic conferences.

I thank Dr. Andrew J. Ewald and Neil M. Neumann for being exceptional collaborators.

Finally, I thank my family and the friends I have made at the University of Waterloo for their support.

Table of Contents

List of Figures

List of Tables

1. Introduction

The diverse structures of many major organs – from the tracheal networks of insects to the lungs, kidneys, and livers of more complex organisms – are constructed from tissues of differentiated cells (Affolter et al., 2003). Epithelial cells are the fundamental building block of these tissues and may become malignant in carcinomas (Hanahan & Weinberg, 2011). Although the spatial organization of organs and the genetic requirements for their formation are relatively well defined (Andrew & Ewald, 2010; Costantini & Kopan, 2010), the connections between gene expression, molecular activities, cell motile behaviours, and tissue structure are incompletely understood (Figure 1). For example, numerous transcripts and genes exclusively expressed in the mammary gland – the milk-secreting ductal breast tissue – and their immediately adjacent stroma have been identified by array-based expression profiling (Sternlicht, Kouros-Mehr, Lu, & Werb, 2006). However, the mechanics of how epithelial cells move and rearrange to form the mammary gland – a process known as epithelial or branching morphogenesis – is not well understood. Improving our understanding of how cells move during regulated epithelial morphogenesis is not only of interest to developmental biology for the purpose of filling gaps in knowledge, but it can contribute to an enhanced understanding of the pathologically dysregulated cell movements during the early stages of cancer metastasis progression.

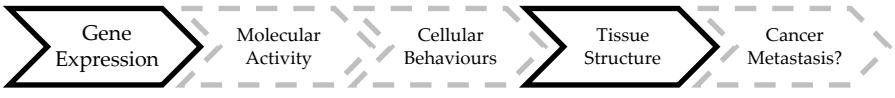

Figure 1. Epithelial Tube Morphogenesis Knowledge Cascade

Numerous transcripts and genes have been identified as responsible for the spatial organization of organs. However, the molecular activities and cellular behaviours connecting gene expression

and organ formation, and the resulting impact this could have on our understanding of cancer metastasis, are incompletely understood.

Branching morphogenesis of the mammary gland is a model system because many of the major molecular mechanisms that underlie its morphology appears to be conserved in all branched epithelial tissues despite differing in final structure and function (Sternlicht, 2006). The mammary gland is an extensive network of branched epithelium that produces and distributes milk from mother to newborn (Sternlicht et al., 2006) and it is the primary site of invasive ductal carcinoma. The homeostatic mammary epithelium is comprised of a single, apico-basally polarized luminal epithelial cell layer surrounded by a single myoepithelial cell layer, thus producing a bilayer (Sternlicht et al., 2006). Branching morphogenesis begins with the stratification and depolarization of the luminal epithelial cells by asymmetric cell divisions (Ewald et al., 2012; Huebner, Lechler, & Ewald, 2014). Next, the branch elongates into the extracellular matrix (ECM) despite the absence of ECM-directed protrusions (Ewald, Brenot, Duong, Chan, & Werb, 2008) and the stratified luminal epithelium returns to a single, apico-basally polarized layer in a process called polarization. Figure 2 shows the branching program for 3D *in vitro* organotypic cultures of murine mammary glands.

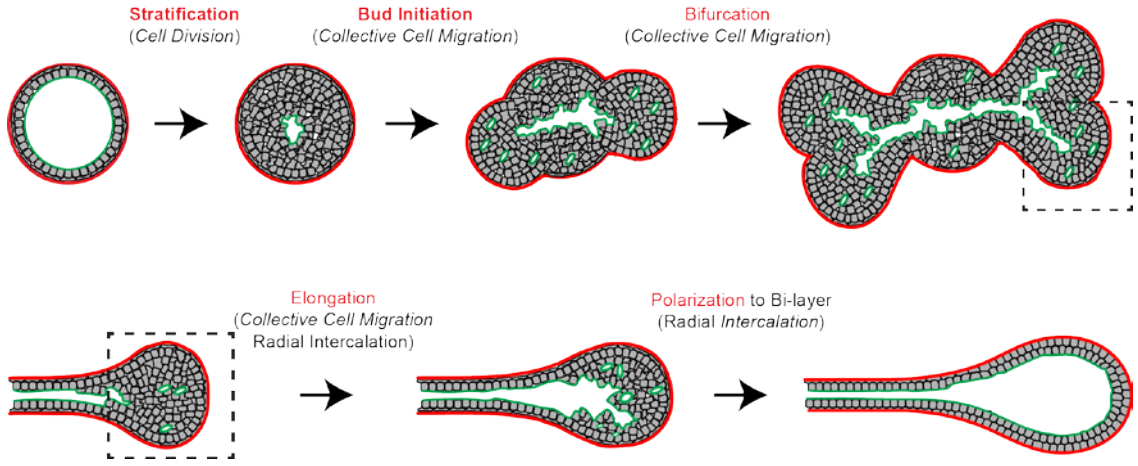

Figure 2. *In Vitro* Branching Morphogenesis Program
(courtesy of Neil M. Neumann)

In vitro branching morphogenesis progresses from a single-layered epithelium to a stratified and depolarized layer of luminal epithelial cells by asymmetric cell divisions. Small buds initiate from the stratified epithelial layer, then bifurcate into branches, and finally elongate into a duct before polarizing back to a single, apico-basally polarized epithelial layer. Throughout this program, the luminal epithelium is covered by a layer of myoepithelium.

The molecular and physical migration mechanisms of the luminal epithelial cells and how their individual behaviours collectively elongate and polarize the mammary epithelium remain unclear because our understanding of branch progression comes from analyzing the morphologies of the branch tips – known as the terminal end buds (TEBs) – at single instances in time rather than continuous observation of the branching events (Sternlicht et al., 2006).

3D culture, real-time imaging, and molecular biosensor studies have shown that luminal epithelial cells can migrate apico-basally between each other, known as radial intercalation, to elongate and polarize mammary epithelium. Luminal epithelial cells express Ras, PIP3, and F-actin in anterior protrusions during migration and intercalation. Furthermore, temporal and functional studies revealed that PIP3 enrichment preceded, and could enrich in the absence of F-actin dynamics (Neumann et al., In Submission).

The experimental part of this study (Neumann et al., In Submission) reveals much about the molecular aspects of tube formation; however, it does not explain the connections between cell behaviour and tissue structure (Figure 1). Cell movements in the context of embryogenesis and wound healing underwent major advances when their mechanical aspects were investigated in addition to molecular studies. Computational modeling revealed conditions in which neural tube defects can arise through mechanical changes in neural plate convergent extension induced by genetic mutations. For example, neural tube defects arose in computational models when convergent extension of the neural plate was reduced by only 20% (Brodland, Chen, Lee, & Marsden, 2010). Computational modeling also showed that the forces responsible for the movement of epithelial cells into damaged areas during wound healing arose from tensions transmitted by a heterogeneous actomyosin ring to the underlying substrate through focal adhesions (Brugues et al., 2014).

Detailed mechanical studies of branching morphogenesis have been lacking, and the purpose of this study is to use computational analysis and modelling to understand the mechanics of the cell movements associated with this process and to connect this understanding to known molecular activities and tissue structure (Figure 1). Specifically, force inference software called CellFIT-3D will be used to analyze 3D imaging of *in vitro* cells to determine the interfacial tensions associated with the proposed molecular activities and cellular behaviours responsible for driving mammary epithelial tube morphogenesis. Then finite element (FE) modeling will be used to test the sufficiency of the identified interfacial tensions to drive epithelial tube morphogenesis. Finally, a

prediction model will be proposed in which cell motility behaviour may be predicted solely be force inference.

2. Background

2.1 Mammary Epithelial Morphogenesis *in Vivo*

First, the structure of the mammary gland is discussed. In mice, the mammary epithelium originates in utero from a multi-layered structure (the mammary placode) which invaginates and establishes a bulb-shaped bud (the mammary rudiment) at the site of each future nipple (Figure 2a-c).

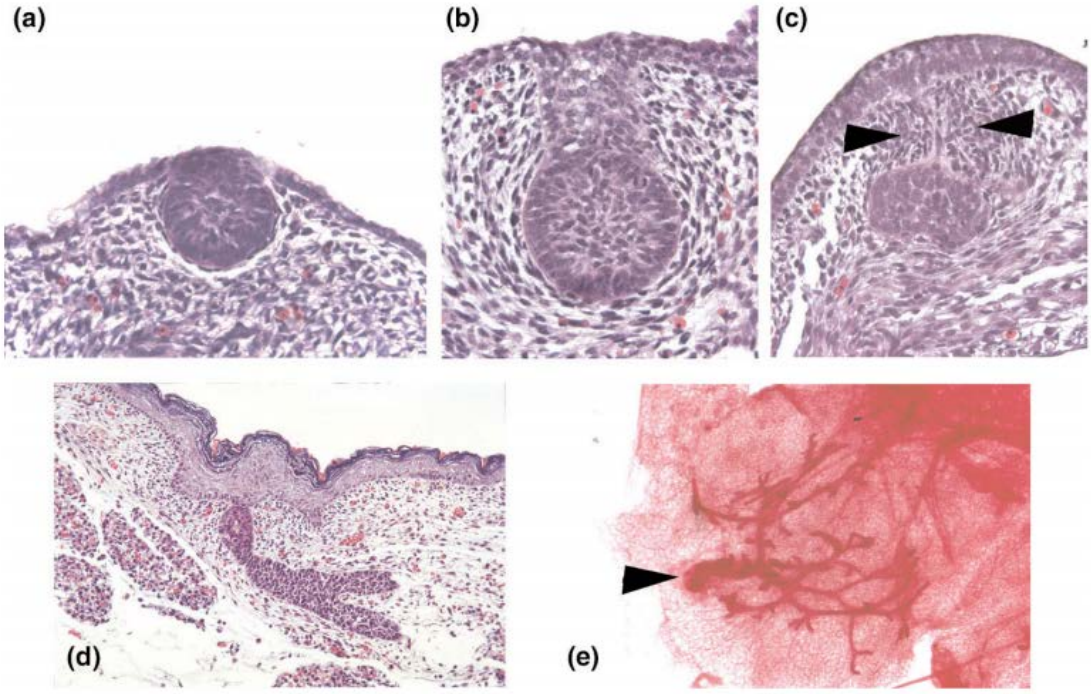

Figure 3. Embryonic Mammary Development
(Hens & Wysolmerski, 2005)

(**a**) Embryonic day (E) 12.5 – epithelial cells have invaginated to form the initial bud. (**b**) Female bud at E14.5 – epithelial cells are arrayed in a ball-on-stalk, or inverted bulb shape. The mesenchymal cells are arranged in four to five layers in a radial fashion around the epithelial cells. (**c**) Male bud at E14.5 – under the influence of testosterone, the mesenchymal cells condense around the stalk of the bud (arrowheads), constricting it until the connection with the surface epidermis is severed. (**d**) Mammary sprout at E18.5 – the epithelial bud has grown out form the mammary mesenchyme into the lower dermis, where it will enter the mammary fat pad. (**e**) Initial primary duct system from a 2-day-old mouse – arrowhead denotes the connection of the primary duct to the skin. Caption from (Hens & Wysolmerski, 2005).

The mammary rudiment elongates, penetrates the underlying mesenchyme, enters the cluster of preadipocytes that becomes the mammary fat pad, and sprouts a limited number of branches prior to birth (Figure 2d,e). This rudimentary ductal tree lies dormant, except for moderate growth to keep up with normal body growth, until puberty when the mammary gland undergoes hormone-dependent branching morphogenesis (Sternlicht, 2006). Bulbous terminal end buds (TEBs) form at the ends of the branches and penetrate farther into the developed fat pad as the duct elongates (Sternlicht et al., 2006). At this point, the mammary gland is composed of two distinct tissue architectures - the first is the bilayered structure, which is composed of inner, luminal epithelial cells, surrounded by contractile myoepithelial cells, further surrounded by a basement membrane (Figure 4). The second tissue architecture is the multilayered TEB (Figure 4).

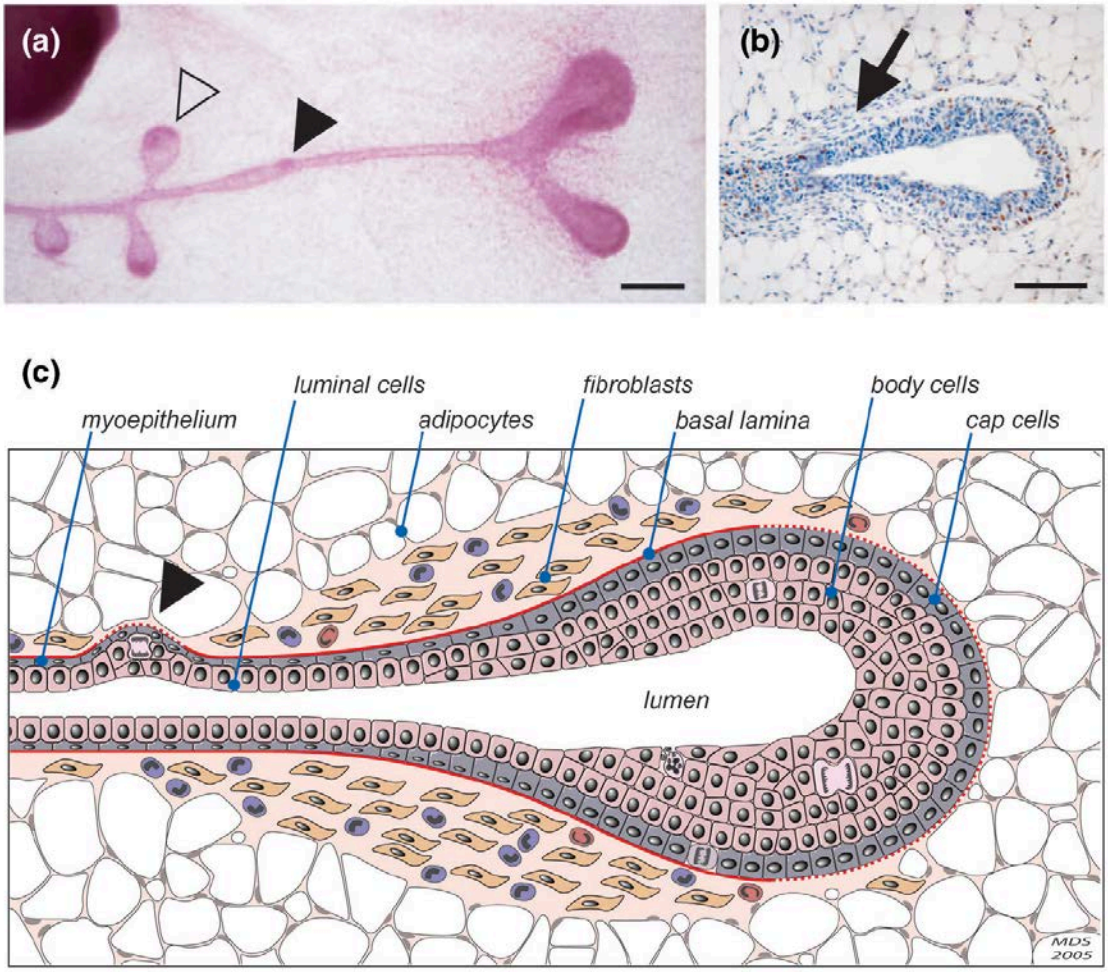

Figure 4. Terminal End Bud (TEB) and Duct Morphology
(Sternlicht, 2006)

(**a**) High-magnification image of a primary duct that has recently passed the central lymph node (upper left corner). Three newly formed lateral (secondary) side-branches are present (open arrowhead). An area of increases cellularity may represent a nascent lateral bud (filled arrowhead). Scale bar is 200 μm. (**b**) Immunophotomicrograph of a TEB illustrating its considerable proliferative activity, as indicated by the large number of cells that have undergone DNA replication (brown diaminobenzidine-stained nuclei). Stroma is rich in fibroblasts and collagen around the collar of the TEB (arrow). Scale bar is 100 μm. (**c**) Schematic diagram depicting the two distinct architectures of a TEB, fibroblast rich stromal collar, and high mitotic index. Caption from (Sternlicht, 2006).

New primary ducts form by bifurcation of the TEBs and secondary side-branches sprout laterally from the trailing ducts until the entire fat pad is filled by an extensive system of branched ducts (Figure 5). Cycling ovarian hormones initiate

the formation of short, tertiary side-branches with lubulo-alveolar structures at their ends (Sternlicht, 2006). Mammary development in humans varies slightly from mice in terms of the number of mammary placodes and rudimentary ductal trees, the absence of surrounding hair pegs, fetal exposure to maternal hormones, and the existence of male mammary rudiment (Sternlicht, 2006); however, these differences are not part of the scope of this study and will not be discussed henceforth. The major mechanisms regulating mammary morphogenesis are likely similar in all mammals.

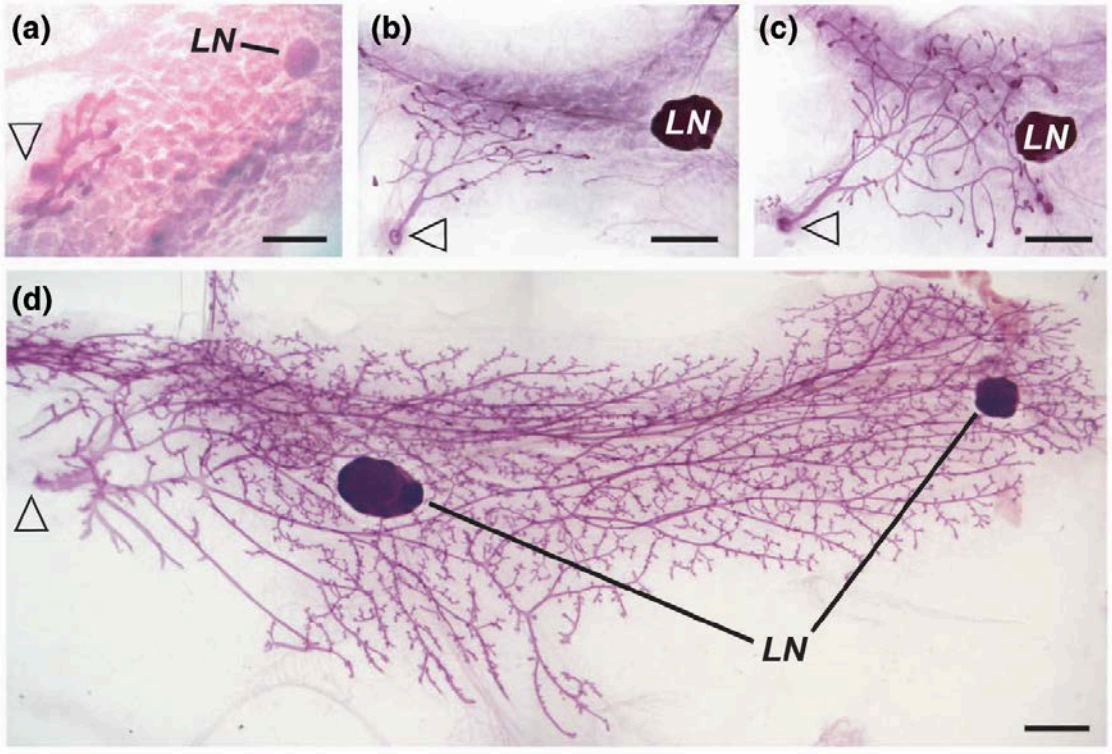

Figure 5. Nuclear-stained Wholemounts Illustrating Ductal Branching Morphogenesis
(Sternlicht, 2006)

(**a**) E18.5, lymph node (LN) in top right corner and main lactiferous duct (arrowhead) on the left. Scale bar is 0.5 mm. (**b**) Age 3 weeks. Scale bar is 1 mm. (**c**) Age 4.5 weeks. Scale bar is 1 mm. (**d**) Age 11 weeks. Scale bar is 1 mm. Caption from (Sternlicht, 2006).

Our understanding of branch progression comes from analyzing TEB morphologies at single instances in time rather than continuous observation of the branching events (Sternlicht et al., 2006). Therefore, the detailed cellular dynamics of TEB elongation and bifurcation remain unclear. Furthermore, numerous transcripts and genes exclusively expressed in TEBs and their immediate adjacent stroma have been identified by array-based expression profiling (Sternlicht et al., 2006). Therefore, the weighted contributions of the ducts and TEBs to the formation of new branches remain unknown. For example, the duct may elongate and push the TEB forward. Alternatively, the TEBs may drive forward giving rise to the trailing ducts (Sternlicht et al., 2006), similar to how one would lay down railroad tracks. Another possibility is that both tissue architectures contribute to branch formation. Time-lapse imaging of embryonic kidney cultures in which the epithelium was labelled with green-fluorescent protein (GFP) provided major insights into the progression of bifurcation and trifurcation in kidney development and the roles of the branch tips and trunks (Shakya, Watanabe, & Costantini, 2005; Watanabe & Costantini, 2004). Therefore, time-lapse imaging of branching morphogenesis may be the key to uncovering the cellular dynamics of mammary development.

2.2 Mammary Epithelial Morphogenesis *in Vitro*

Unlike many mechanical systems, biological systems have active semi-autonomous control systems that alter the mechanics from one moment to the next. Therefore, a working knowledge of the molecular signaling pathways that affect sub-cellular structural components is required to understand the mechanics. Observing the molecular and cellular dynamics of mammary development for extended time periods is difficult *in vivo* because elongation

occurs over the course of weeks (Ewald et al., 2008). Therefore, Ewald and colleagues developed 3D organotypic culture techniques to recapitulate branching morphogenesis within ECM gels (Ewald et al., 2008). To do so, the primary murine mammary epithelium was isolated, the mammary gland was digested, and collections of 100-300 epithelial cells (organoids) were isolated and embedded in a 3D ECM to form cysts with a bilayered structure and lumen (Ewald et al., 2008). Cellular dynamics were observed overtime using real-time confocal imaging and molecular biosensors (Ewald et al., 2008).

Addition of FGF2 to the medium induced the cyst lumen to fill with mostly luminal epithelial cells and initiated new branches to elongate through gaps in myoepithelium coverage, followed by myoepithelial migration to restore coverage (Ewald et al., 2008). The elongating duct fronts were always stratified, but reversion to a bilayer was common. The luminal epithelial cells appeared adherent to each other, yet they moved chaotically in the direction of elongation, whereas the myoepithelial cells moved both toward and against the direction of ductal elongation (Ewald et al., 2008). Elongation typically ceased after full coverage by the myoepithelium (ME), whereas ducts typically bifurcated in the presence of partial ME coverage (Ewald et al., 2008). Cells expressing smooth muscle actin were observed at bifurcation sites; however, it could not be determined whether myoepithelial cells induced the bifurcation or responded to a separate decision to bifurcate (Ewald et al., 2008). ME motility closely correlated with changes in duct shape (Ewald et al., 2008). Elongation cessation was accompanied by the TEB transitioning from a stratified to a bilayered epithelium (Ewald et al., 2008). The TEB tips were often free of cells expressing

smooth muscle actin (Ewald et al., 2008). The *in vitro* branching program was illustrated in Figure 2.

Recently, the use of real-time imaging and molecular biosensors was able to build off the work of Ewald and colleagues (Ewald et al., 2008), demonstrating that mammary tubes elongate and polarize through a mechanical process called radial intercalation (Neumann et al., In Submission). First, cavitation by regulated cell death (apoptosis) was considered as a candidate mechanism for bilayer formation (Figure 6A) (Mailleux et al., 2007). If cavitation was the mechanism, it would be expected that selective apoptosis be present in the duct interior, apoptosis would increase as the tubes stopped elongating, and the tubes would fail to polarize when apoptosis was inhibited.

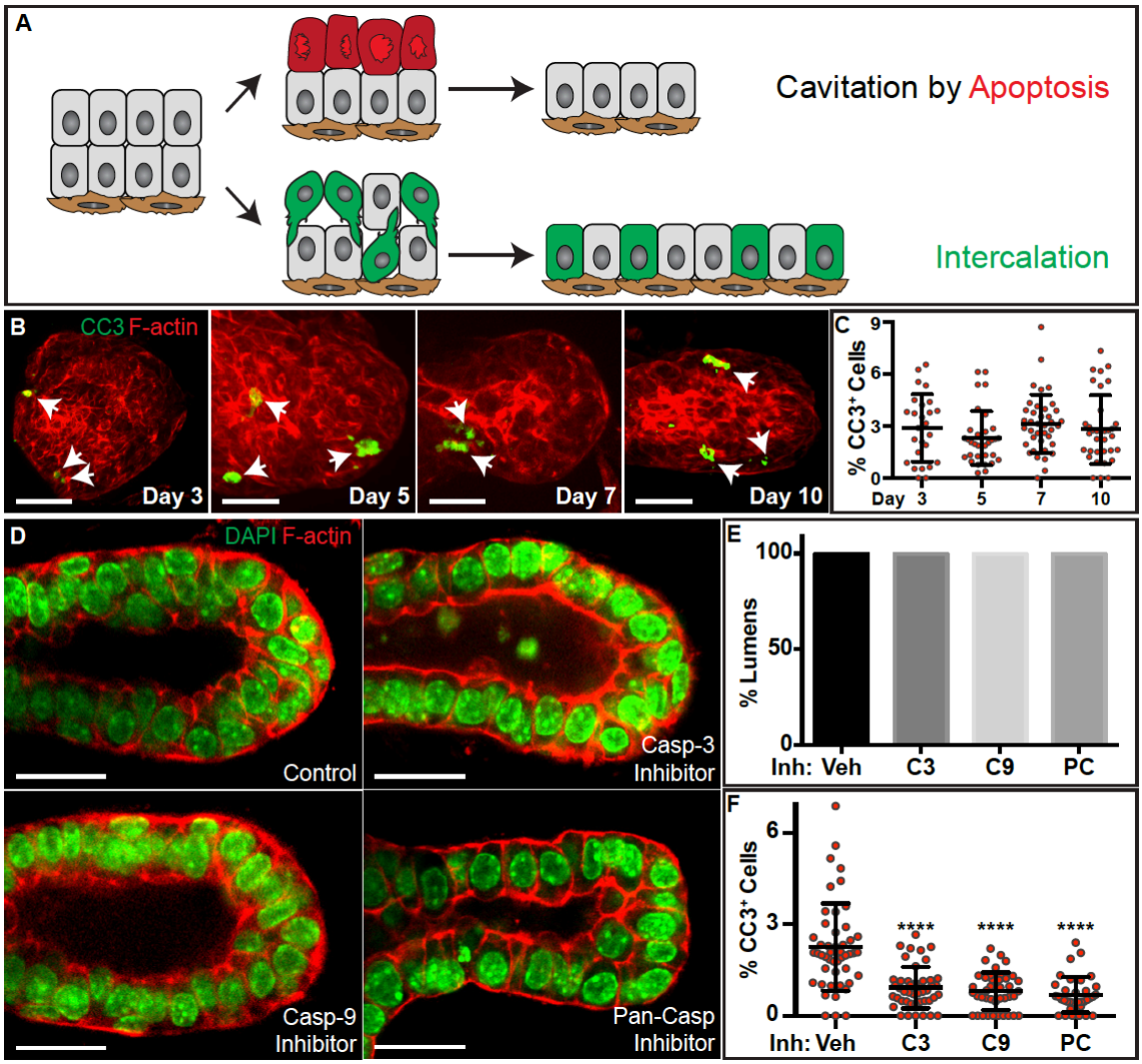

Figure 6. Bilayer Formation Does Not Require Apoptosis
(Neumann et al., In Submission)

(**A**) A bilayer could form by cavitation or intercalation. (**B**) 3D confocal projections of F-actin (red) and cleaved Caspase-3 (CC3, green) from days 3, 5, 7, and 10 in culture. Scale = 20 μm. (**C**) Percent CC3+ cells from day 3 (26 organoids (orgs)), 5 (33 orgs), 7 (39 orgs), and 10 (34 orgs) (mean ± S.D.; r=4). Kruskal-Wallis test did not reach significance ($p > 0.05$). (**D**) 3D confocal projections of membranes (tdTomato, red) and nuclei (DAPI, green) of organoids treated with scrambled peptide control or caspase-3, caspase-9, or pancaspase inhibitor, taken at 10 days. Scale = 20 μm. (**E**) Quantification of lumen formation at 10 days in organoids treated with scrambled peptide control (45 orgs), cleaved caspase-3 (33 orgs), cleaved caspase-9 (33 orgs), or pan caspase inhibitors (48 orgs). r=4. (**F**) Quantification of percentage of CC3+ cells in 3D confocal data. Even focal staining was counted as CC3+. CC3 levels were significantly reduced in each inhibitor condition (caspase-3 (0.93%, 35 orgs), caspase-9 (0.81%, 45 orgs), and pan caspase (0.69%, 40 orgs)), compared to vehicle (2.25%, 48 orgs) (mean ± SD; r=4). Kruskal-Wallis test reached significance ($p < 0.0001$). Caption from (Neumann et al., In Submission).

To test these predictions, the distribution of apoptotic cells were analyzed during branch elongation and polarization. Neither, interior enrichment of apoptotic cells (Figure 6B), nor an increase in apoptosis were detected during polarization (Figure 6B,C). Therefore, neither the location nor timing of apoptosis suggested cavitation as the primary mechanism. Next, the requirement for apoptosis to complete polarization was tested by treating organoids with apoptosis inhibitors (Figure 6D-F) and imaged in 3D. Each inhibitor reduced apoptosis (Figure 6F) but every organoid exhibited clear lumens and polarized architecture, across conditions (Figure 6D,E) (Neumann et al., In Submission). Therefore, apoptosis was not required for bilayer formation.

Radial intercalation, a process where cells migrate between layers (Walck-Shannon & Hardin, 2014), was tested as an alternate mechanism of thinning a multilayered tissue. Unlike cavitation, intercalation into basal positions would increase the surface area of the tube and contribute to elongation. Green fluorescent protein (GFP)-expressing cells within mosaically labelled organoids (Figure 7A) were tracked to determine whether intercalation occurred during mammary branching (Neumann et al., In Submission).

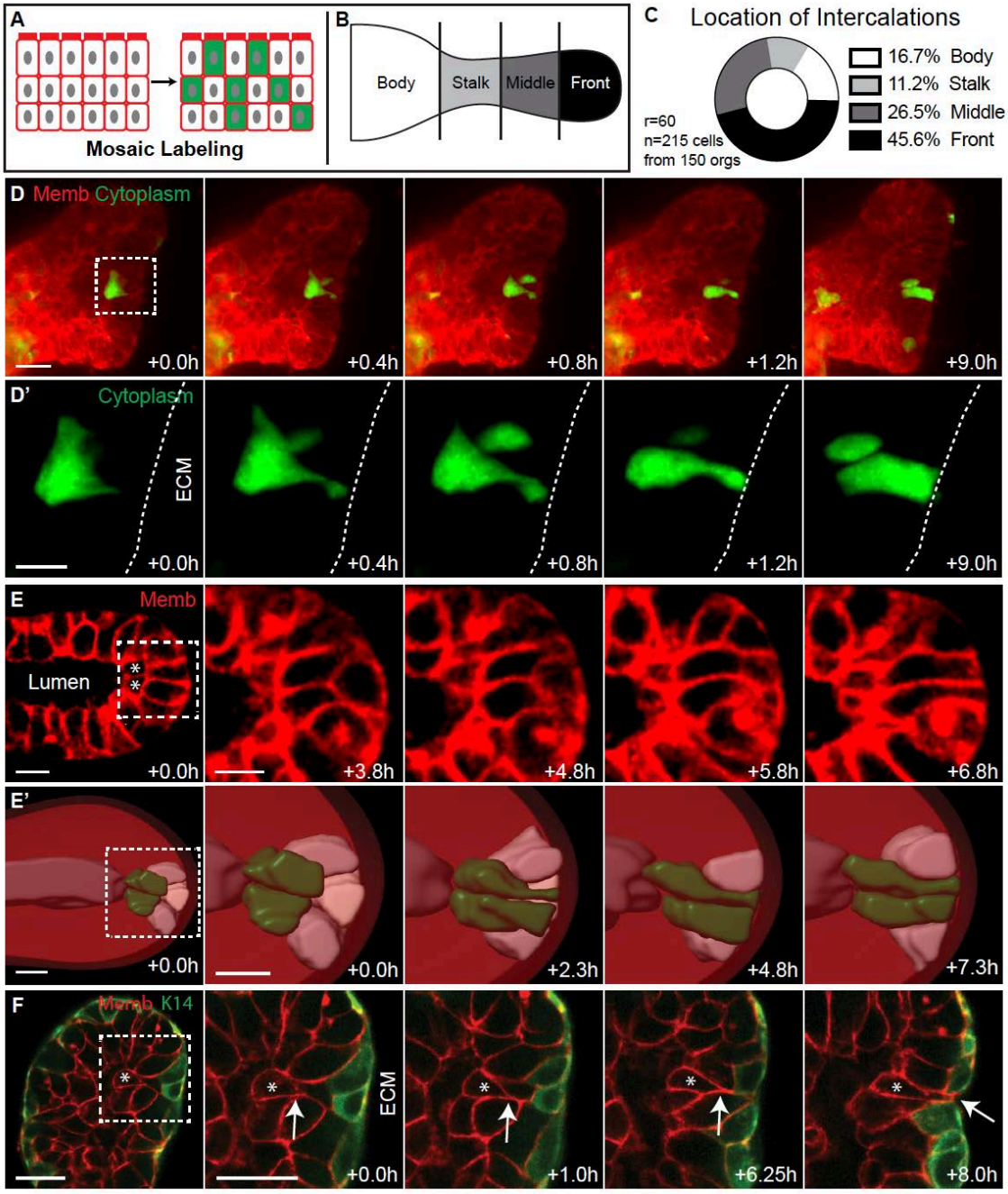

Figure 7. Radial Intercalation Occurs During Duct Elongation and Bilayer Formation

(Neumann et al., In Submission)

(**A**) Organoids with ubiquitous membrane labeling were mosaically infected with GFP. (**B**) Elongating branches were divided into body, stalk, middle, and front regions. (**C**) Intercalations were quantified based on location in body (36), stalk (24), middle (57) or front (98) regions. (215 cells, r=60 from 150 orgs). (**D**) (**D'**) 3D confocal projections of a cell migrating, intercalating and transitioning to columnar morphology during branch elongation (membranes (tdTomato, red);

cytoplasm (GFP, green). Scale = 20 μm in (**D**) and 10 μm in (**D'**). (**E**) A single plane from a 3D confocal time-lapse showing a branch that is bilayered except for 4 cells in the front (white box). The two cells touching the lumen intercalate to contact the basal surface and complete the bilayer. (**E'**) 3D surface rendering of the cell movements in (**E**) (Surfaces function; Imaris). Scale = 10 μm. (**F**) A single plane from a 3D confocal time-lapse showing an intercalating cell contacting the myoepithelium (membranes = red, myoepithelium = green). Scale = 20 μm. Caption from (Neumann et al., In Submission).

Cells were observed undergoing migration and radial intercalation to contact the basal surface in all four regions of the elongating branch (Figure 7B), with a majority of intercalations in the front or middle (215 intercalations, 150 organoids; Figure 7C-D'). Furthermore, radial intercalation was observed to resolve a multilayer to a bilayer (Figure 7E,E', stars). Both migrating and intercalating cells were observed to have a characteristic 'tear-drop' cell morphology defined by a singular anterior protrusion and rounded posterior (Figure 7D' 0.4h, E' 2.3h, F 1h). As luminal epithelial cells radially intercalate they make direct contact with the myoepithelium (Figure 7F, star) (Neumann et al., In Submission).

Next, the molecular signalling pathway responsible for epithelial migration and intercalation was investigated and determined to be tyrosine kinase (RTK, Figure 8A), the same pathway that governs mammary branching (Neumann et al., In Submission; Sternlicht et al., 2006). Using FGF2 as the ligand, molecular activity was assayed using fluorescent biosensors and binding domains at key points along the tyrosine kinase signally pathway (Figure 8A). The first point in the pathway that was observed was an upregulation of Ras activity in anterior protrusions during migration (Figure 8B, arrowheads) and intercalation (Figure 8C, arrowheads), which were consistent with the types of molecular asymmetries observed at the front of migratory single cells (Neumann et al., In Submission).

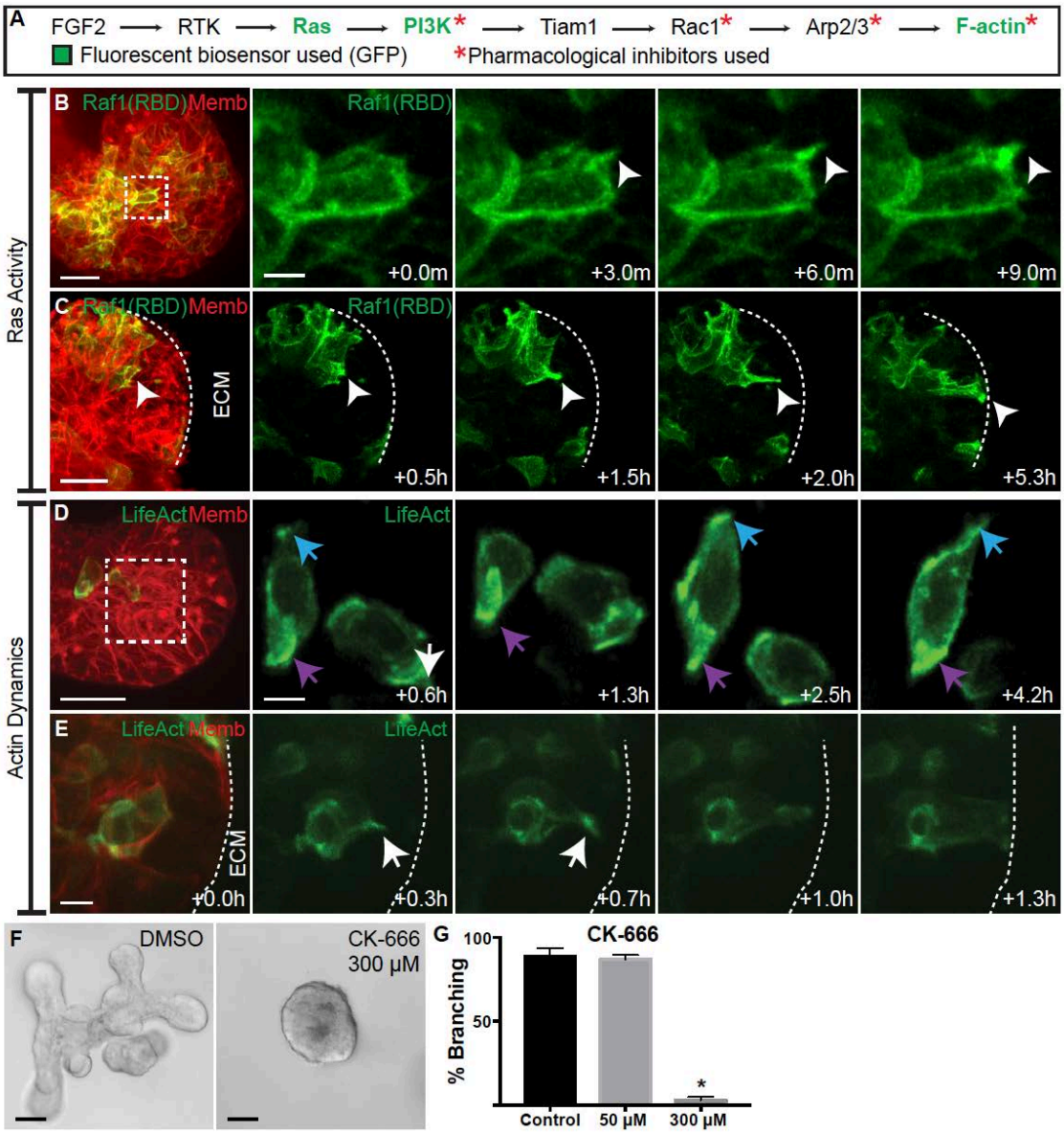

Figure 8. Epithelial Protrusions Enrich Ras Activity and F-actin Polymerization (Neumann et al., In Submission)

(**A**) Receptor tyrosine kinase schema indicating biosensors and inhibitors used. (**B**) A migratory cell enriches Ras activity to its protrusion (Raf1-(RBD)-GFP, green; membrane, red). N=210 cells from 16 orgs, r=3. Scale = 20 µm (5 µm inset). (**C**) An intercalating cell enriches Ras activity to its anterior membranes (Raf1-(RBD)-GFP, green; membrane, red). N=10 cells from 28 orgs, r=4. Scale = 20 µm. (**D**) Migratory cells enrich F-actin to new protrusions (white and blue arrows) and display posterior enrichment of F-actin (purple arrows) (LifeAct-GFP, green; membrane = red). N=176 cells from 73 orgs, r=4. Scale = 20 µm (5 µm inset). (**E**) An intercalating cell enriches F-actin polymerization to its anterior protrusion (LifeAct-GFP, green; membrane = red). N=26 from 73 orgs, r=4. Scale = 20 µm. (**F**) Organoids were treated with DMSO or Arp2/3 inhibitor (CK-666) from Day 0 of culture, imaged at Day 7. Scale = 50 µm. (**G**) Quantification of percent branching in

organoids treated from Day 0 with DMSO (88.7±4.8%, 403 orgs), 50 μM CK-666 (87.1±2.5%, 522 orgs), or 300 μM CK-666 (2.9±1.9%, 425 orgs), imaged at Day 7 (r=4; mean ± SD). Caption from (Neumann et al., In Submission).

Knowing that F-actin is the downstream product of the tyrosine kinase pathway (Figure 8A), a biosensor that binds to recently polymerized F-actin (Riedl et al., 2008) was used to show F-actin consistently enriched to the protrusions of migratory cells (Figure 8D, blue and white arrows) (Neumann et al., In Submission). This finding suggests Ras recruitment induces F-actin rich protrusions, through the mediation of Rac1 and Arp2/3 (Figure 8A), to cause cytoskeletal changes and alter cell shape. F-actin enrichment observed in the posterior of migratory cells (Figure 8D, purple arrows) suggests rear contractility pairs with anterior protrusions during migration. Actin polymerization preceded deformations of cell shape both as cells initiated and ceased migrating. For example, F-actin was enriched in the anterior protrusion of an intercalating cell as it reached the basal tissue surface and then the anterior actin dissipated as the cell assumed a columnar shape (Figure 8E, white arrowheads). These dynamics were consistent with a transition from migratory front-rear to stationary apico-basal polarity. The requirement for Arp2/3 in regulating F-actin polymerization during branching morphogenesis was tested using an inhibitor. Treated organoids were viable but unable to initiate new branches (Figure 8F,G) (Neumann et al., In Submission).

The final critical signalling node linking Ras activity and actin polymerization is PI3K (Figure 8A) and its molecular activity was observed using a biosensor that localizes to regions of PIP3 enrichment. PIP3 biosensor accumulation was observed in the protrusions of migratory and intercalating cells (Figure 9A,C).

PI3K activity was dynamic for several minutes (Figure 9A) and membrane enrichment persisted for approximately one hour or longer (Figure 9C). Enrichment was typically prior to or concurrent with protrusion extension (Figure 9B). Furthermore, a dose dependent block of branching was observed, testing the requirement for PI3K activity (Figure 9D,E) (Neumann et al., In Submission).

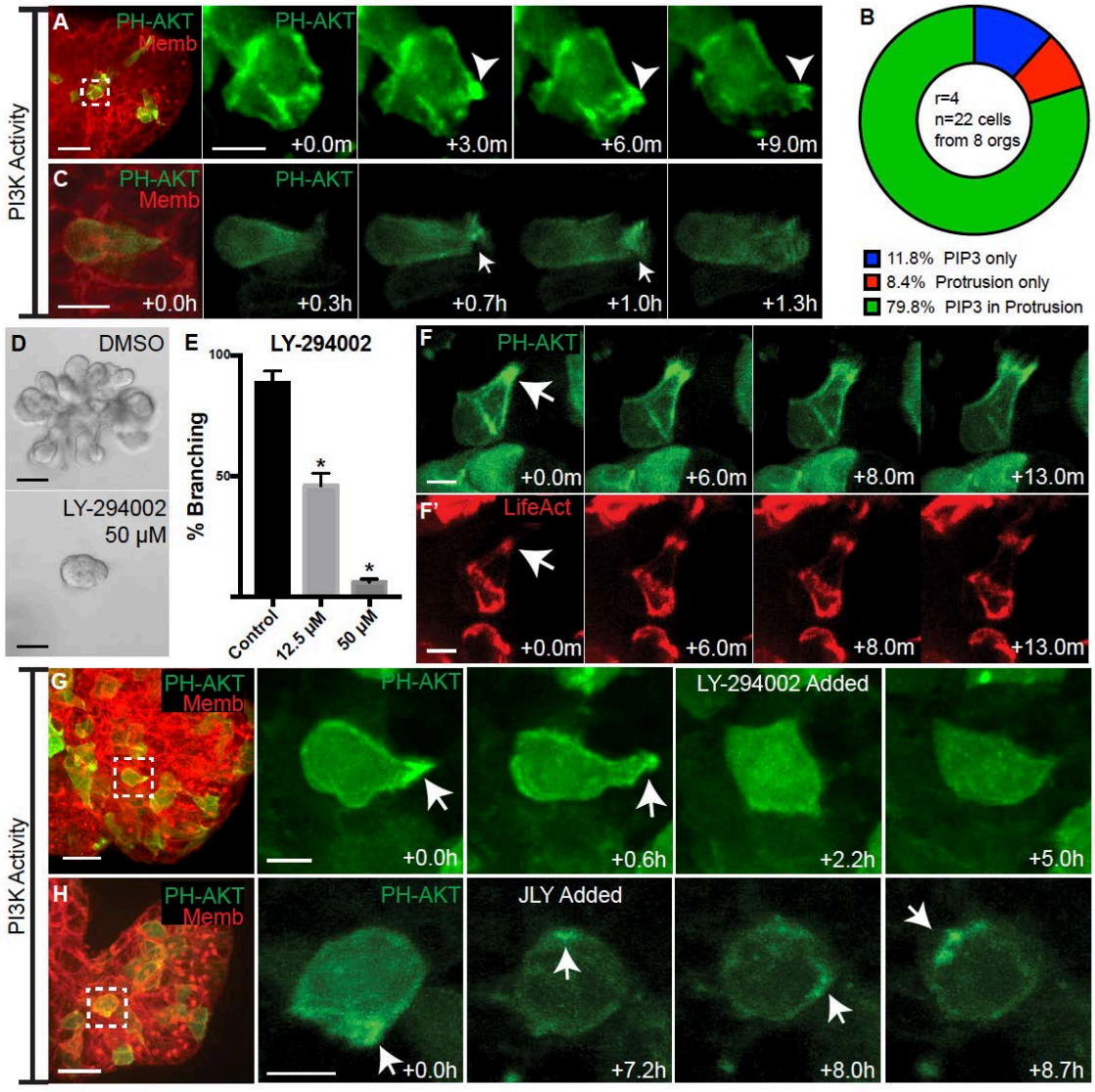

Figure 9. Epithelial Protrusions Enrich and Require PI3K Activity (Neumann et al., In Submission)

(**A**) A migratory cell enriches PI3K activity to its protrusion (PH-Akt-GFP, green; membrane, red). N=150 cells from 10 orgs, r=3. Scale = 20 μm (5 μm inset). (**B**) Quantification of isolated PIP3 (11.8%), protrusion without PIP3 (8.4%) or PIP3 in a (**C**) An intercalating cell enriches PIP3 to its anterior protrusion (PH-Akt-GFP, green; membrane, red). N=30 from 131 orgs, r=6. Scale bar is 5 μm. (**D**) DIC images of organoids treated with DMSO or 50 μM PI3K inhibitor (LY-294002) from Day 0. Scale = 5 μm. (**E**) Quantification of branched organoids treated at Day 0 with DMSO control (87.1±2.5%, 403 orgs), 12.5 μM LY-294002 (46.1±5.2%, 530 orgs), and 50 μM LY-294002 (6.1±1.3%, 514 orgs) (r=4; mean ± SD). (**F**) (**F'**) An intercalating cell enriches PIP3 and F-actin polymerization within a protrusion, with the peak of PIP3 signal occurring first (PH-Akt-GFP, green; LifeAct-RFP, red) . N=10 cells from 25 orgs, r=3. Scale = 5 μm. (**G**) A migratory cell enriches PIP3 and generates a protrusion (white arrowhead; PHAkt-GFP, green; membrane, red). PI3K inhibition (50 μM LY-294002) resulted in loss of PIP3 biosensor from the membrane and collapse of protrusions. N=416 cells from 16 orgs, r=1. Scale = 20 μm (5 μm inset). (**H**) A migratory cell enriches PIP3 and generates a protrusion (white arrowhead; PHAkt-GFP, green). Jasplakinolide, Latrunculin A, and Y27632 (JLY) treatment induced retraction of protrusions and cell rounding. Dynamic membrane enrichment of PIP3 continued (white arrows) but did not lead to protrusions. N>1,000 cells from 65 orgs, r=4. Scale = 20 μm (5 μm inset). protrusion (79.8%). N=22 cells from 8 orgs, r=4. Caption from (Neumann et al., In Submission).

Finally, mosaically co-infected organoids with a PI3K biosensor and an F-actin biosensor were used to determine whether PI3K signaling leads to F-actin polymerization and migratory cell dynamics. The peak of PI3K activity typically preceded the peak F-actin signal (Figure 9F, F', arrows). PI3K inhibition led to the retraction of existing protrusions, and an absence of new protrusions (Figure 9G) (Neumann et al., In Submission).

Inhibitors targeting actin depolymerization, polymerization, and contractility were used to disconnect the PI3K signaling axis completely from its ability to influence or respond to actin dynamics (Neumann et al., In Submission; Peng, Wilson, & Weiner, 2011; Wang, Artemenko, Cai, Iglesias, & Devreotes, 2014). Following addition of the inhibitors, cells lost their protrusions, adopted a rounded morphology, and failed to extend new protrusions. However, they continued to enrich PI3K activity to focal regions of the plasma membrane (Figure 9H) (Neumann et al., In Submission). This data agreed with analyses of

chemotaxis in *Dictyostelium discoideum* where the peak of PI3K activity preceded the peak of actin polymerization and inhibition of actin dynamics did not prevent PI3K enrichment (Devreotes & Horwitz, 2015). This suggests that PI3K signaling leads to F-actin polymerization and migratory cell dynamics.

Ultimately, the tyrosine kinase signalling pathway (Figure 8A) was essential to cells migrating and intercalating to the basal surface. These motile cells were characterized by 'tear-drop' cell shape with F-actin enriched in the anterior protrusion and cell posterior. The anterior actin dissipated as the cell assumed a columnar shape. However, it remains unclear if the downstream products of the tyrosine kinase signalling pathway are sufficient to drive the cellular behaviours required to construct mammary epithelial tubes (Figure 10). Without this information, the use of mammary epithelial tubes as a model system for improving our understanding of epithelial tube morphogenesis, in general, or diseases such as cancer metastasis, is limited.

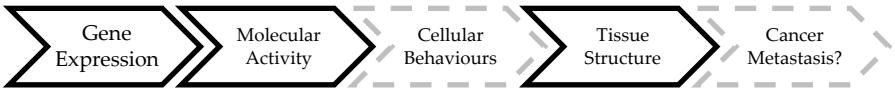

Figure 10. Mammary Epithelial Tube Morphogenesis Knowledge Cascade
The tyrosine kinase molecular pathway has been identified as responsible for the spatial organization of mammary epithelial tubes, and radial intercalation has been proposed as the cellular behaviour. However, radial intercalation has not been shown to drive tube formation.

2.3 Cell Mechanics and Computational Modeling

Computational models provide a useful platform within which cellular mechanisms can be tested for their potential role in tissue level developmental processes. In this study, computational models will be used to test whether

branching morphogenesis can be driven by F-actin enriched migrating and intercalating cells. However, a discussion detailing the mechanical structures of the cell, the mechanism driving cell self-rearrangement, and the types of computational models is required to continue.

The cell membrane is composed of a selectively permeable phospholipid bilayer and it is under tension due to the intracellular pressure from the cytoplasm and organelles it contains. Scattered about the membrane are transmembrane and surface proteins that connect the membrane to various interior structural elements (cytoskeleton) and other cell membranes (Figure 11) (Cowin & Doty, 2006). The cytoskeleton is a network of fibrous proteins that maintain cell shape, mechanical strength of the cell, support and intracellular transport of organelles, and chromosome separation during cell division (Cowin & Doty, 2006; Ethier & Simmons, 2007). The three primary classes of fibrous protein are microfilaments, intermediate filaments, and microtubules.

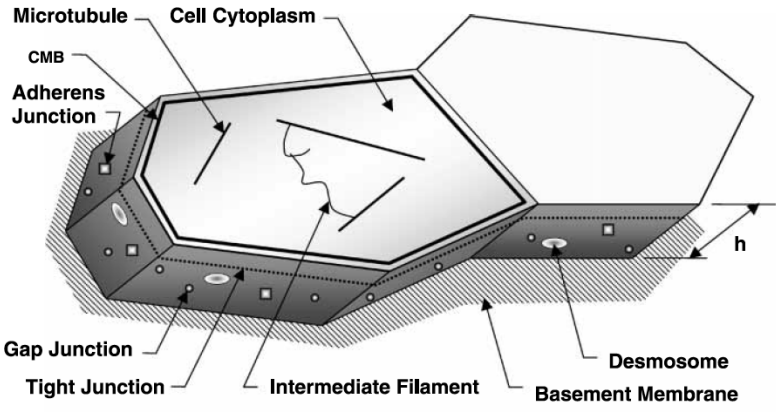

Figure 11. Structural Components of Epithelial Cells
(Brodland, Viens, & Veldhuis, 2007)
A schematic representation of two cells and their structural components that are assumed to form part of an epithelium.

Microfilaments are composed of the protein monomer actin. A layer of antiparallel, mutually sliding actin filament polymers (F-actin) connected by myosin bridges (Beloussov, 1994) is located in the subcortical region of the cell (Cowin & Doty, 2006). Actin is also present in bundles surrounding the apical end of embryonic cells of some species (Beloussov, 1994; Odell, Oster, Alberch, & Burnside, 1981) and criss-crossing the cell, which reinforces the cortical action. The microfilaments contract, generating tensile forces along the cell membrane. Apical bundles of microfilaments in neighbouring cells can act in concert to create contractions over large distances along a tissue (Cowin & Doty, 2006).

Intermediate filaments make up a network of stabilizing fibres that provide mechanical strength and integrity to the cell by bracing the microfilaments, microtubules, and organelles (Cowin & Doty, 2006). Microtubules are composed of actin monomers, provide structural rigidity, aid in cell motility, transport agents for proteins and organelles within the cell, and aid in shape changes during cell division (Cowin & Doty, 2006).

The mechanisms driving cell self-rearrangements such as embryonic development, morphogenetic process, and wound healing can be described mechanically through experiment or computational modeling (Brodland, 2004; Brodland et al., 2010; Brugues et al., 2014; Harris, 1994). Wilson first observed cell sorting in sponges by dissociating cells and observing them reassemble into functional organisms (Harris, 1994). Wilson concluded the observed movements must have occurred to reassemble the cells and the forces driving sorting must have come from the cells (Harris, 1994). Townes and Holtfreter performed

experiments in morphogenesis where neural cells were arranged in varying starting configurations with other cell types. They observed that the aggregate tended to have the same final geometry independent of the starting configuration. This finding suggested that similar physical mechanisms were responsible for engulfment, invagination, and cell sorting (Harris, 1994). Brodland showed that infolding of the neural plate is driven by acto-myosin contractility on the apical surface of the neural plate (Brodland et al., 2010; X. Chen & Brodland, 2008; Clausi & Brodland, 1993).

The Differential Adhesion Hypothesis (DAH) was the first theory to describe the nature of the mechanical forces that drive cell self-rearrangement. DAH proposes that cells behave like immiscible liquids. Cells with higher cell-cell adhesion sort to the interior of others just as liquids will do based on relative intermolecular adhesion (Steinberg, 1962). DAH is supported by three sets of observational evidence (Steinberg, 1970):

1. Transitive hierarchy. If cell type A engulfs cell type B, and cell type B engulfs cell type C, then cell type A will engulf cell type C.
2. A certain cell type will be engulfed by another cell type if it can sort internally to that other cell type.
3. Those cell types which sort more internally are also more resistant to flattening out of aggregates of their type.

The Differential Interfacial Tension Hypothesis (DITH) proposes that interfacial tensions, acting tangent to cell-cell interfaces, cause local displacements at cell junctions which lead to motion and rearrangements at the cell and tissue levels (Brodland, 2002). DITH suggests that cell-cell adhesions contribute to surface contractility similar to how molecular adhesion results in an apparent contractile

film on the surface of liquids (Harris, 1994). The observational evidence supporting DAH can be explained by cortical contractility and DITH. Item #1 holds for any theory based on quantitative difference, item #2 indicates that the mechanism for sorting is similar to that of engulfment, an observation also made by Townes and Holtfreter, and item #3 suggests that the mechanism for rounding up is similar to that of sorting and engulfment (Brodland, 2004; Brodland, 2002; Harris, 1976). Many other researchers agree that cell self-rearrangement is the result of the interplay between adhesion and surface tension (Hilgenfeldt, Erisken, & Carthew, 2008; Krieg et al., 2008; Lecuit & Lenne, 2007; Rauzi, Verant, Lecuit, & Lenne, 2008). The forces of the mechanical components of two cells (A and B, arbitrarily) can be superimposed to a net interfacial tension

$$\gamma_{AB} = F_A^{Cyto} + F_B^{Cyto} + F_A^{Mem} + F_B^{Mem} - F_{AB}^{Adh} + F_{AB}^{Other} \quad (1)$$

where the term F_A^{Cyto} and F_B^{Cyto} account for forces oriented along the membrane from the cytoplasm, apical microtubules, and intermediate filaments of cells A and B, respectively. The terms F_A^{Mem} and F_B^{Mem} represent the membrane and cortical actin layer tension of cells A and B, respectively. The term F_{AB}^{Adh} includes the adhesion force between cells A and B generated by the cell adhesion molecules (CAM) and reduces the tension along the interface. The term F_{AB}^{Other} accounts for any other contractile forces along the interface between the two cells (H. H. Chen & Brodland, 2000).

There are several models for the mechanical behaviour of cells and tissues. At the single-cell level, lumped parameter visco-elastic models, including Maxwell and

Kelvin bodies, are 1D mechanical circuits describing the behaviour of a single cell. Multiple elements may be used to construct multicellular aggregates and tissues (Ethier & Simmons, 2007). Tensegrity structures are a network of compression and tensile elements used to model the cytoskeleton (Ethier & Simmons, 2007). At the multicellular level, lattice models or cellular automata use single or multiple (sub-cellular lattice) sites in square or hexagonal lattices to represent cells. Randomly, an algorithm selects a cell and one of its neighbours, a measure of the change in free energy of the system is calculated, and a decision is made whether or not to change the pair of cells. Lattice models have been used to model cell sorting (Cowin & Doty, 2006; Glazier & Graner, 1993).

Centric models derive cells from forming points distributed over the domain of interest. The number of forming points is controlled and each forming point gives rise to an individual cell through the use of a Dirichlet or Voronoi tessellation. For each time step, the incremental forming point displacements that cause the largest change in free energy and balance the energy dissipation caused by the cell viscosity are calculated and cell neighbour changes may result (Brodland, 2004). Vertex models define polygonal cells by the spatial coordinates of their vertices. A cell boundary is randomly chosen and its ends are moved to minimize the sum of its length and the cell boundaries framing into it without changing the areas of the two cells sharing the selected boundary (Brodland, 2004).

2.4 Finite Element Modeling

In this study, 2D finite element (FE) models (Brodland & Chen, 2000; Brodland, 2006; Brodland & Veldhuis, 2006; Brodland et al., 2007; H. H. Chen & Brodland,

2000) will be adapted and used to test whether branching morphogenesis can be driven by F-actin enriched migrating and intercalating cells. FE modeling is the technique of dividing an object of interest into sufficiently small elements whose behaviours can be modeled mathematically. The Brodland FE model follows DITH and mathematically describes the relationship between the displacements and forces within patches of cells over time. Each cell is represented as an individual element made of nodes, edges, and a viscous dashpot system. Adjacent cells share nodes and edges. Nodes are points in space that correspond to the junction of three cell membranes, called a triple junction, and may displace in the x- and y-direction to satisfy force equilibrium. Closely spaced triple junctions approximate nodes that may otherwise connect four or more cell edges together – quad junctions and rosettes, respectively. Edges model the interface between two cells, or between a cell and the medium, and the forces acting along them. Each edge is assigned a tension based on the nature of the interface (H. H. Chen & Brodland, 2000).

The interfacial tensions are generated by the mechanical components of the cell, including cell membrane proteins, microfilaments, and cell-cell adhesion systems, and are modeled using a constant-force rod element (H. H. Chen & Brodland, 2000) (Figure 11). During tissue remodelling processes such as sorting and embryogenesis, cells undergo strain rates on the order of 10^{-6}/s. Therefore, the cell cytoplasm, organelles, and filamentous networks are assumed to be passive and modeled as a massless, viscous, incompressible fluid using an orthogonal dashpot system. The orthogonal dashpots are oriented along the major and minor axes of the cell. Each dashpot is connected to one node and to a

common ground (Brodland et al., 2007). The dashpots along the major axis are illustrated in Figure 12.

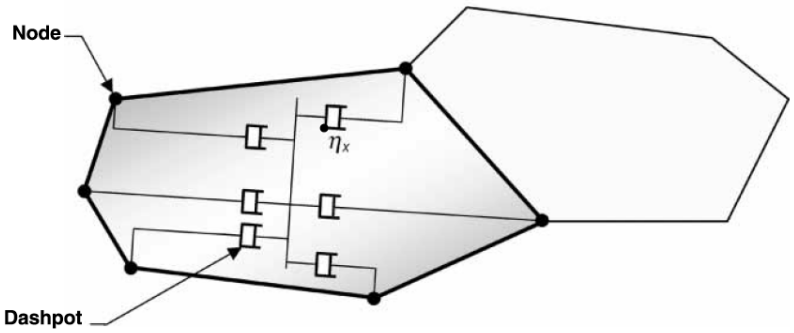

Figure 12. Orthogonal Viscous Dashpot System
(Brodland et al., 2007)
In the interest of image clarity, only the dashpots aligned with the long axis of the cell are shown. The second set of dashpots would run orthogonal to those shown.

The effective viscosity is defined by

$$\mu_A = \frac{4g\pi\mu hB}{nA} \tag{2}$$

where g is a form factor equal to 0.682, μ is the effective cell viscosity, n is the number of nodes which comprise the cell, h is the cell thickness, and A and B are the major and minor axes of the cell, respectively (Brodland et al., 2007). Displacement, velocity, force, stress, or area constraints may be imposed on the model. The area of each cell may be held constant for modeling the cell contents as incompressible. For example, planar sheets of cells conserve area through motion (Hutson et al., 2009; Odell et al., 1981). All model constraints are imposed as Lagrange side conditions to the equation of motion. The general equation of motion is given by

$$M\ddot{u} + C\dot{u} + Ku = f_m + f_c + f_k \quad (3)$$

where the scale of biological cells is sufficiently small to neglect mass M and inertial forces f_m, the cell elasticity K and associated forces f_k are neglected because of the small strain rate, and the equation of motion reduces to Equation 4 when the nodal velocities $\dot{u}$ are substituted for the nodal displacements u divided by the time increment and $f_c = f$.

$$C\left(\frac{1}{\Delta t}u\right) = f \quad (4)$$

The vector sum of interfacial tensions F framing into each node is calculated and placed into Equation 4 with the corresponding contributions from the viscous dashpot systems C (Brodland et al., 2007; H. H. Chen & Brodland, 2000). Solving the system of equations yields the incremental nodal displacements that produce viscous forces in the cytoplasm that balance the interfacial tension forces. The locations of the nodes are updated and the mathematical procedure is repeated for the next time increment. The resulting solution vector also produces the Lagrange multipliers associated with the constraints for current time step. The Lagrange multipliers for constrained degrees of freedom (DOF) such as nodal displacement or velocity constraints are the reaction forces at those DOF. These are the forces required to maintain equilibrium of the patch at each node. The Lagrange multipliers for the volume constraints on each cell correspond to the

internal pressure or viscous forces required for that cell to maintain its volume and be in dynamic equilibrium with the membrane tensions.

Consistent with what is observed experimentally, cells change contact neighbours when interfaces become sufficiently short (H. H. Chen & Brodland, 2000; Eaton & Julicher, 2011; Walck-Shannon & Hardin, 2014). When a boundary between two cells in the model reaches a specified minimum length, typically 2.5% of an average cell diameter, that boundary will be eliminated and a new boundary will be created between the two cells that were previously separated by the short edge length. The new boundary is given a length longer than the specified minimum to ensure that that neighbour change does not reverse in the next time step (H. H. Chen & Brodland, 2000).

2.5 Measuring and Inferring Forces in Cells

Several experimental techniques for obtaining information about the forces driving cell motion exist. Thin glass rods inserted into cells to apply force or constrain neutral movements (Rappaport, 1977), atomic force microscopes that exert known forces and measure displacements (Thomas, Burnham, Camesano, & Wen, 2013), micropipette aspirations that measure surface tension (Maitre et al., 2012), and substrate deformation techniques that measure traction forces (Legant et al., 2010; Tambe et al., 2013) belong to a group of techniques applicable only to cells positioned on the surface of a mass or cells in a monolayer epithelium accessible to physical contact. These techniques are not applicable to the interior of cell aggregates or to tissues protected by a basement membrane, as is the case with the *in vitro* organoids (Ewald et al., 2008).

Magnetic cytometry in which magnetic forces are applied to inserted ferrous particles (Kasza, Vader, Koster, Wang, & Weitz, 2011), morphological techniques based on the shapes of inserted oil droplets (Campas et al., 2014), optical tweezers that exert forces on endogenous or injected particles with different refractive indices (Capitanio & Pavone, 2013), FRET techniques that aim to report deformations and forces by optical means (Borghi et al., 2012; Morimatsu, Mekhdjian, Adhikari, & Dunn, 2013), and laser ablation techniques that determine deformations and forces by measuring recoil rates belong to a group of techniques that provide force information for specific locations and times. However, it is difficult to provide force information for an entire cell aggregate over time.

Forward model equations that calculate motions from forces may be inverted and used to estimate forces from shapes and motions under suitable conditions and with appropriate side conditions. Video Force Microscopy (VFM) uses inverse methods to construct detailed maps of the forces driving ventral furrow formation in *Drosophila* (Brodland et al., 2010; Cranston, Veldhuis, Narasimhan, & Brodland, 2010). VFM showed the initial stages of ventral furrow formation are driven by apical constrictions that arose smoothly over time and varied with medio-lateral position at the invagination site. These findings were unlike the step functions often assumed in conceptual and computational models (Conte, Muñoz, Baum, & Miodownik, 2009). However, inverse methods are limited by their high sensitivity to noise, a ubiquitous problem in image digitalization, and solver issues brought on by poor equation stability. Reducing the number of unknown variables by assuming all cells had the same intracellular pressure (Chiou, Hufnagel, & Shraiman, 2012) and using Bayesian solvers to address

equation stability issues (Ishihara & Sugimura, 2012) are examples of techniques devised to mitigate the issues associated with inverse methods.

The Cellular Force Inference Toolkit (CellFIT) treats cell boundaries as being curved, which substantially improves equation stability and reduces noise sensitivity. This technique assumes that cell-cell interfacial tensions are the primary drivers of cell shape and motion because cell motions are assumed to be sufficiently slow to neglect viscous forces. Force-balance equations are constructed and solved at the triple junctions (2D) or curvilinear triple edges (3D) where three cells meet. The cell-cell interfacial tensions are assumed to be uniform between pairs of adjacent triple junctions or triple edges and intracellular pressure within each cell is assumed to be constant. This technique can be used for single images (2D) (Brodland et al., 2014), confocal image stacks at a specific time point (3D) (Veldhuis et al., 2017), or through time (4D) (Veldhuis et al., 2017).

Regardless of the spatial and time domain, a coherence filter may be used to smooth crenulated and poorly defined cell-cell interfaces at the pixel-level (Figure 13a-d). A coherence filter was not used in this study. Cells of interest are then segmented using a watershed algorithm (Figure 13e,f) (Mashburn, Lynch, Ma, & Hutson, 2012). In 2D, a circular arc is fit to the pixels corresponding to each cell-cell interface to estimate the edge curvature and the angles at which the edge approaches its triple junction (Figure 13h,i) (Brodland et al., 2014). In 3D, segmented outlines in successive sections are grouped by the cells to which they belong and used to reconstruct the triple edges (Figure 13g). Planes are constructed normal to spline-based approximations of these curvilinear edges

and geometric projection techniques used to reconstruct the dihedral angles of the cells in these planes (Figure 13l,m). In ascertaining these angles, the cell boundaries are assumed to be curved, and local curve fitting is used to obtain best approximations of these angles in each plane (Figure 13i,k). Data from multiple planes along each triple edge is used so as to optimize the angle measurements and confirm their reliability (Veldhuis et al., 2017).

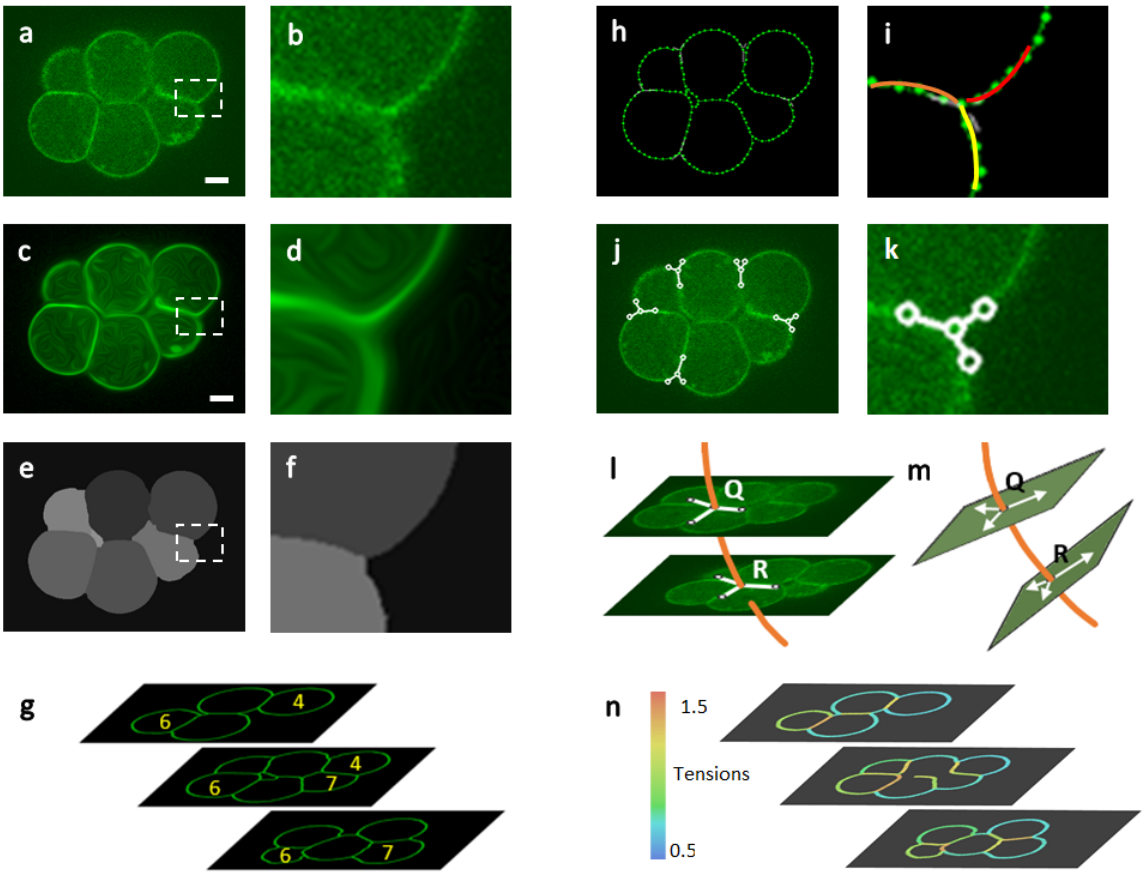

Figure 13. CellFIT Overview
(Veldhuis et al., 2017)

(**a**) A raw confocal image of an eight-cell stage murine embryo. Scale bar, 10 mm. (**b**) An enlargement of the boxed area. (**c**) An edge enhancing coherence filter was used to smooth the boundaries. (**d**) Edge enhancing coherence filter closes the gaps. Parameters used: Scheme, implicit discretization; total diffusion time ¼ 25; Gaussian sigma ¼ 3. (**e**) and (**f**) SeedWater-segmented cells, each denoted by in a different intensity of grey. (**g**) Corresponding cells in successive images were grouped together and triple edges that appeared in multiple images identified. (**h**) A fine mesh was constructed along each cell boundary. (**i**) Approach angles to any

given triplet determined by circular arc fitting. (**j**) and (**k**) Tangent vectors were calculated automatically and adjusted manually as needed. (**l**) Splines were fit through the triplets that appeared in successive images. (**m**) Dihedral planes and angles calculated. (**n**) Least-squares equations were constructed, solved, and calculated tensions displayed. Caption from (Veldhuis et al., 2017)

Cell-cell interfaces behave mechanically, like a membrane, carrying no bending or shear stress and rely on tensions along their shape to carry load. Figure 14A illustrates the membrane and its associated forces in 2D (Brodland et al., 2014).

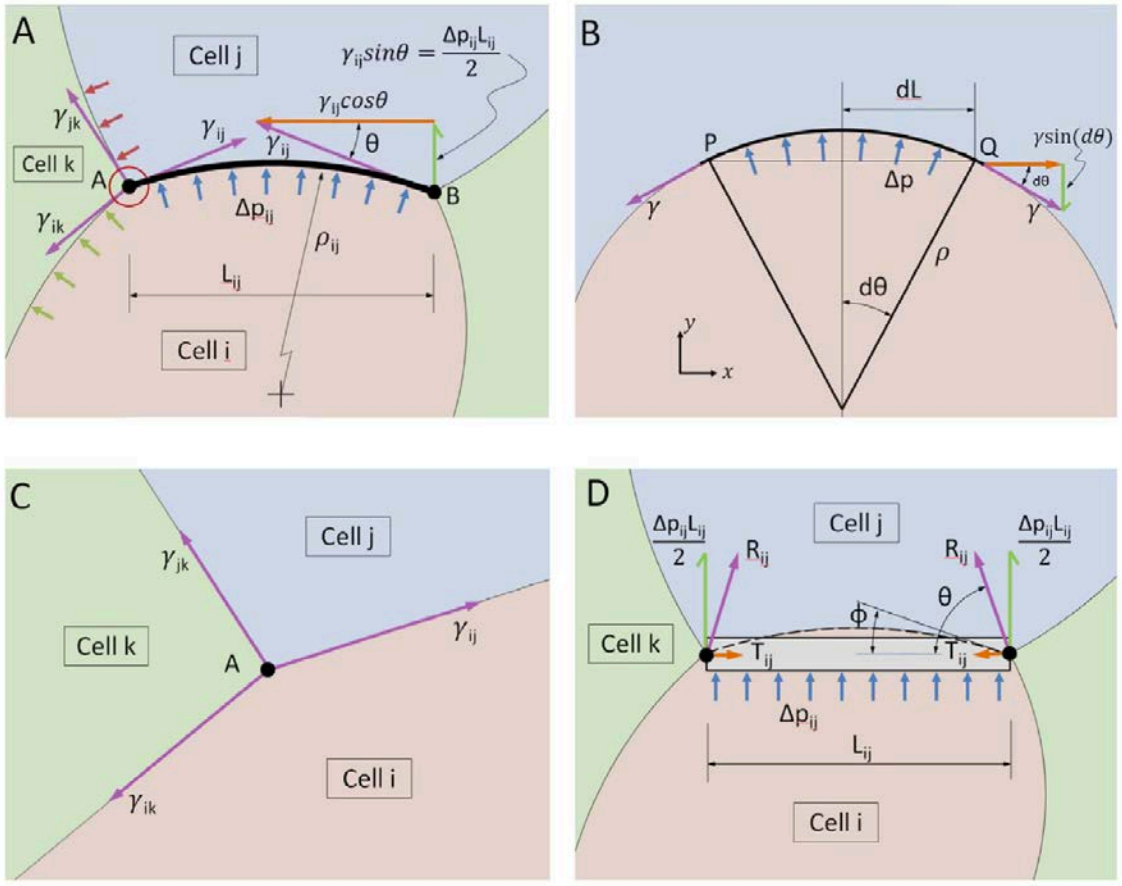

Figure 14. Equilibrium Considerations in Force Inference (Brodland et al., 2014)

(**A**) A curved cell edge and the forces acting on it. (**B**) Relationship between edge tension, curvature and pressure. (**C**) The forces acting at a typical triple junction. (**D**) The forces acting on an edge that is constrained to remain straight by beam action.

The geometry of the membrane changes to accommodate a change in load. The relationship between the pressure difference Δp_{ij} across a given membrane, radius of curvature ρ_{ij}, and interfacial tension γ_{ij} is defined by the Laplace equation

$$\Delta p_{ij} = {}^{\gamma_{ij}}/_{\rho_{ij}} \tag{5}$$

The tension in the membrane increases as the pressure difference across the membrane increases when the curvature of the membrane is held constant. If the pressure difference is constant, the radius of curvature will increase proportionally as the tension in the membrane increases. In the special case where there is no pressure difference across the membrane, it would still carry tension but have an infinitely large radius of curvature. The assumption of uniform tension along the membrane would need to be modified if loads with force components tangent to the membrane were applied (Brodland et al., 2014).

The vector force γ_{ij} of a cell edge tension acting on a triple junction acts in the direction of the final limiting angle at which the cell edge approaches the triple junction. For any particular triple junction to be in equilibrium, the adjacent cell edges must satisfy

$$\sum \gamma_{mn} \hat{r}_{mnA} = 0 \tag{6}$$

where the unit vectors $\hat{r}_{mnA}$ are constructed tangent to the limiting angle at which the membrane along the boundary between cells m and n approaches the

A_{th} triple junction and pointing away from the junction, and the summation is carried out over all edges that connect to that triple junction. The γ_{mn} values are the corresponding unknown membrane tensions. The pressure forces do not need to be accounted for in Equation 6 by considering Figure 14C which represents a very small region around the triple junction labelled A, and identified by a small red circle in Figure 14A. As the region of interest is made smaller, the length over which pressure forces normal to any given membrane can act becomes vanishingly small and its force contribution becomes negligible (Brodland et al., 2014).

Conversely, straight cell edges must act as beams carrying both bending and shear in order to remain straight (Hibbeler, 2011). The pressure loading Δp_{ij} gives rise to shear forces of magnitude $\Delta p_{ij} L_{ij}/2$ at each end of the beam. The beam can also carry tension T_{ij}. The vector sum of the shear force and tension force R_{ij} may not be tangent to the membrane at the triple junction and this is the apparent reason that straight edge-based approaches tend to encounter computational challenges such as high noise sensitivity (Brodland et al., 2014). One situation where this non-alignment is not a problem, however, is when the edges of cells are essentially perpendicular to each other as was the case when VFM was used to study ventral furrow formation (Brodland et al., 2010).

The angle measurements at each triple junction (2D) or triple edge (3D) give rise to a pair of equilibrium equations that relate the relative tensions in the three cell-cell interfaces that meet there. The tensions acting along these interfaces are assumed to be isotropic and constant, the pairs of equations arising from the

various triple junctions or triple edges may be related to each other, and a master set of simultaneous equations may be produced by

$$G_\gamma \gamma = 0 \tag{7}$$

where matrix G_γ contains cosines or sines relating to the equilibrium equations at each triple junction or triple edge and the vector γ contains the interfacial tension magnitudes. These equations are sufficiently overdetermined to allow exclusion of a limited number of cell edges that are short, poorly imaged, crenulated, or incomplete. The system of equations is solved in a constrained least-squares sense (Equations 8 and 9) to avoid producing a trivial solution, improve the solution accuracy, verify the mutual compatibility of the various dihedral angle equations, assess the power of the available equations to offer a trustworthy solution and estimate the accuracy of the tension calculated for each cell-cell interface.

$$\begin{bmatrix} G_\gamma^T & C_1^T \\ C_1 & 0 \end{bmatrix} \begin{Bmatrix} \gamma_1 \\ \vdots \\ \gamma_{N_{Tensions}} \\ \lambda_1 \end{Bmatrix} = \begin{Bmatrix} 0 \\ \vdots \\ 0 \\ N_{Tensions} \end{Bmatrix} \tag{8}$$

where

$$C_1 = \{1 \quad \cdots \quad 1\} \tag{9}$$

Here, the system is constrained such that the mean of the interfacial tension magnitudes equals 1 and λ_1 is the Lagrange multiplier associated with this

constraint. Alternatively, external information may be used to scale the solution (Brodland et al., 2014; Veldhuis et al., 2017).

3. Tool Development

Sections 3.1 and 3.2 of this chapter consist of work paraphrased from a paper that has been submitted for publication (Neumann et al., In Submission). Section 3.2 also consists of work paraphrased from a published paper (Perrone, Veldhuis, & Brodland, 2015).

3.1 CellFIT-3D Modifications

To determine the relative interfacial tensions associated with cell migration and intercalation, CellFIT-3D (Veldhuis et al., 2017) was modified. The migrating cell and its immediately adjacent neighbours were segmented using a watershed algorithm (Mashburn et al., 2012). Typically, large patches of cells would be analysed; however, a limited number of cells were selected for analysis to mitigate the influence of error provided by poorly defined cell boundaries that are not of particular interest. Cell boundaries in confocal images may seem well defined; however, noise, gaps, and other anomalies become apparent at the pixel level (Veldhuis et al., 2017). An enhanced coherence filter may be used to amend the poorly defined cell boundaries; however, this technique and others like it, still introduce error into the analysis when calculating the angles at which interfaces join together (Veldhuis et al., 2017). Local changes in F-actin were observed on the interfaces between the migrating cell and the cells it is migrating between. When determining the driving forces associated with cell migration, one is particularly interested in the interfacial tensions local to the migrating cell. Therefore, analyzing a smaller patch of cells is the chosen approach to mitigating imaging error when it can be afforded to do so, as is the case with cell migration (Neumann et al., In Submission).

Segmented outlines in successive sections were grouped by the cells to which they belong, as explained elsewhere (Figure 13g). Cubic splines were fitted to the cell segments to form meshes with uniformly-spaced mesh points (Figure 13h). Points in the mesh where three segmented cells meet (triplets) represent the points at which the 3D curvilinear junctions (triple edges) pass through the confocal section (Veldhuis et al., 2017). The in-plane angles at which cell-cell interfaces approach a triplet were calculated by fitting separate circular arcs to the last 5 mesh points (Figure 13i) and shown graphically by, overlaying on the confocal image, a circle at the calculated triplet location and vectors in the calculated approach directions (Figure 13j,k). Manual angular adjustments were made to the graphical triplet vectors, as needed. 3D splines were fitted through groups of three or more triplets belonging to the same triple edge (Figure 13l).

At each triplet location along the triple edge, vectors were mapped onto local dihedral planes constructed normal to the spline (Figure 13m) and a pair of equilibrium equations, defining the ratio of cell-cell interfacial tensions that satisfies equilibrium at the particular location along the triple edge, was formulated for two arbitrary orthogonal directions (Veldhuis et al., 2017). The tensions acting along these interfaces are assumed to be isotropic and constant (Veldhuis et al., 2017). The paired equilibrium equations were checked for consistency with other equation pairs belonging to the same triple edge, eliminated if the dihedral plane is strongly tilted, such may be the case at spline ends, averaged into one pair of equations for each triple edge, and assembled into the homogenous system of equations presented earlier (Equation 7). The system of equations is solved in a constrained least-squares sense similarly to how it was presented earlier (Equations 8 and 9); however, the constraints were

modified. Localized F-actin changes were observed in an anterior protrusion and the posterior of a migrating cell. It is reasonable to assume that if there are changes in interfacial tension, they will occur along these interfaces. Therefore, the other interfacial tensions in the observed patch of cells were set to have magnitudes of one instead of constraining the system such that the mean of the interfacial tension magnitudes equals one (Neumann et al., In Submission).

3.2 FE Model Modifications

The intercalating cells in the *in vitro* organoids (Ewald et al., 2008) have curved and convoluted shapes. However, virtually all cell-level computational models have approximated cell-cell interfaces as being straight, although cell-medium interfaces are often treated as curved or polygonal (Brodland, 2004; Glazier & Graner, 1993; Honda, 1978; Staple et al., 2010). Modelling internal edges as straight would seem to be a reasonable approach given that cell–cell interfaces are only slightly curved in many situations, including the one illustrated in Figure 15A. However, it was discussed previously that assuming cell-cell interfaces to be straight required the cell edges to act like beams carrying both bending and shear. The vector sum of the shear force and tension force may not be tangent to the membrane at the triple junction and this is the apparent reason that straight edge-based force inference approaches tend to encounter computational challenges such as high noise sensitivity (Brodland et al., 2014). This impasse led to the development of CellFIT, which relies on accurate cell–cell contact angles and interface curvatures. Testing CellFIT required the development of computational models that could generate configurations with curved edges represented as connected line segments, called polylines (Brodland et al., 2014).

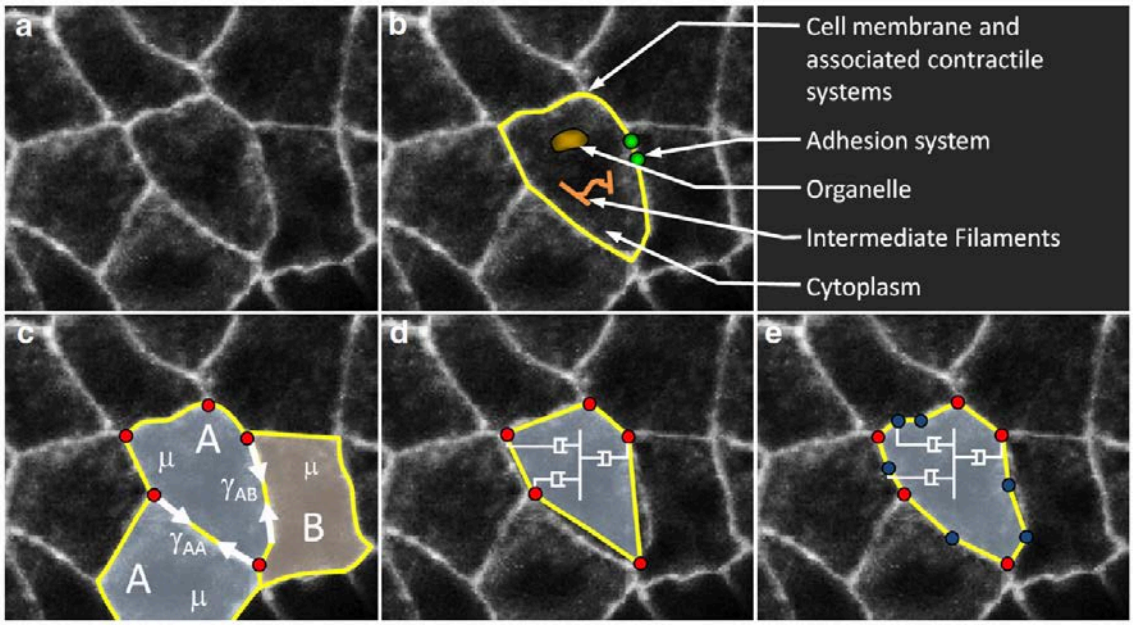

Figure 15 An Epithelium and Its Corresponding Monoline and Polyline Models (Perrone et al., 2015)

(**a**) An image of amnioserosa cells in a *Drosophila* embryo during early dorsal closure (courtesy of M. Shane Hutson). (**b**) Primary functional and force-generating structures. (**c**) The net interfacial tensions γ acting along the cell boundaries and the effective viscosity μ of their cytoplasm. For explanatory purposes only, the cells are considered to be of two types and the tensions associated with different kinds of boundaries are labelled with subscripts. (**d**) Monoline model of the system in (**c**) and straight rod elements (shown in *yellow*) are used to represent each cell edge and to carry its interfacial tension γ. Select *dashpots* representing the effective cytoplasm viscosity μ are shown. Notice that nodes (*red dots*) exist only at the triple (or higher-order) junctions. (**e**) The associated polyline model and its segmented edges have multiple rod elements connected by intermediate nodes (shown in *blue*). Note how the segmented edges much more closely approximate the true cell shapes. Caption from (Perrone et al., 2015).

A study was conducted to describe the mathematical and computational foundations of the polyline model, to investigate contact angle, cell shape, and cell motion discrepancies between straight-edge (monoline) and polyline models, to determine whether these discrepancies are a direct result of the straight-edge assumption, and to address whether the mechanical flexibility that curved edges essentially afford to cells facilitates certain kinds of behaviour *in silico*. Framework was created to help modellers choose an appropriate model for

studying specific phenomena. This framework will be used to select the appropriate model for branching morphogenesis.

Like its monoline counterpart, the polyline model assumed epithelial cells (Figure 15A) derive their mechanical properties from cytoskeletal components and from other structural elements (Figure 15B). The active forces generated by cell membrane and actomyosin contraction, and ameliorated by cell-cell adhesion systems were combined into a net interfacial tension γ that is tangent to the cell boundary (Figure 15C) (Brodland, 2002; Lecuit & Lenne, 2007). In the monoline model, the net interfacial tension is embodied in a single straight constant-force rod element (Figure 15D) (Brodland et al., 2007; H. H. Chen & Brodland, 2000). However, multiple rod elements associated with a particular edge were assumed to carry the same tension in the polyline model (Figure 15E). The number of intermediate nodes could be adjusted at will, and they were created or removed as the simulation progressed so as to produce segments that were no longer than one-quarter of an average cell diameter. This criterion produced approximately 2 or 3 intermediate nodes per edge on average and was found to produce motions and shapes essentially the same as those that had more, suggesting that shape convergence had been achieved (Perrone et al., 2015).

The cytoplasm, organelles and filamentous networks inside each cell were assumed to play a passive role, generate an effective viscosity μ (Figure 15C), and modelled using the same orthogonal dashpot system (Brodland et al., 2007) discussed earlier. Part of the dashpot system is shown schematically in Figures 15D,E. When calculating the dashpot coefficients from cell geometries with intermediate nodes, the denominator used in that calculation must contain not

the number of nodes n in the cell as in Equations 8 and 9 of (Brodland et al., 2007), but the number of triple junction nodes plus half of the total number of intermediate nodes. The fact that the intermediate nodes should be weighted by one-half was determined using patch tests (Irons & Shrive, 1983), and this result was found to be appropriate for cells with up to 10 intermediate nodes per side on average, cytoplasm that was not necessarily incompressible (i.e., not restrained to a Poisson's ratio of $\nu = 0.5$), and aspect ratios (Brodland, Chen, & Veldhuis, 2006) as high as 4 (well beyond the normal range of cell shapes). A definitive analytical argument for this experimentally determined weighting factor was not identified (Perrone et al., 2015).

Both models were run for a fixed number of time steps of specified size. For each time step, the global force vectors and the effects of the dashpots in each cell are assembled and the incremental displacements of each node are calculated in the same manner described earlier (Brodland et al., 2007; H. H. Chen & Brodland, 2000). The intermediate nodes in the polyline model are treated in exactly the same way as the triple junction nodes when carrying out these calculations. Also, the polyline model contains the same neighbour change algorithms described earlier (H. H. Chen & Brodland, 2000). An embargo timer is also sometimes used, as in the tissue engulfment studies reported here, to prevent any new edges with high tensions from spontaneously shortening and changing back (Perrone et al., 2015).

The length of individual polyline segments also changed as the model ran, and it was often necessary to adjust their number from one time step to the next. When the length of any particular polyline segment was larger than the user-specified

maximum, typically 25% of a cell diameter, it was divided into two line segments of equal length with a new intermediate node between them (Perrone et al., 2015). Should a particular polyline segment become smaller than a specified minimum length, typically 2.5%of a cell diameter, the nodes at its ends were merged into one node. If both nodes were intermediate nodes, the new node was placed in the middle of the old line segment. If one was an intermediate node and the other a triple junction, the intermediate node was simply merged with the triple junction node (Perrone et al., 2015). If both nodes were triple junctions, that edge is assumed to be governed by the neighbour change criterion described previously (H. H. Chen & Brodland, 2000). All models were verified using patch and convergence tests (Irons & Shrive, 1983).

As discussed earlier, monoline cell edges behave like beams and transfer intracellular loads to their ends because they are forced to remain straight (Brodland et al., 2014). The resulting transverse shear

$$V_{jk} = \frac{1}{2}\Delta p_{jk} L_{jk} \tag{10}$$

at the beam ends, which is proportional to the intracellular pressure difference Δp_{jk} and the side length L_{jk}, must be added to the beam tension γ_{jk} to obtain the total load from the interface between cells j and k (Figure 16A). In the polyline model, an edge is made of multiple segments (Figure 16B) and the shear load becomes a fraction of the value found in monoline model since the length L_{jk} decreases. As the number of polyline segments increases, the shear force V_{jk} decreases until, in the limit as the segment lengths approach zero length, it

disappears. Therefore, the polyline edge tends to behave more like a membrane than a beam (Perrone et al., 2015).

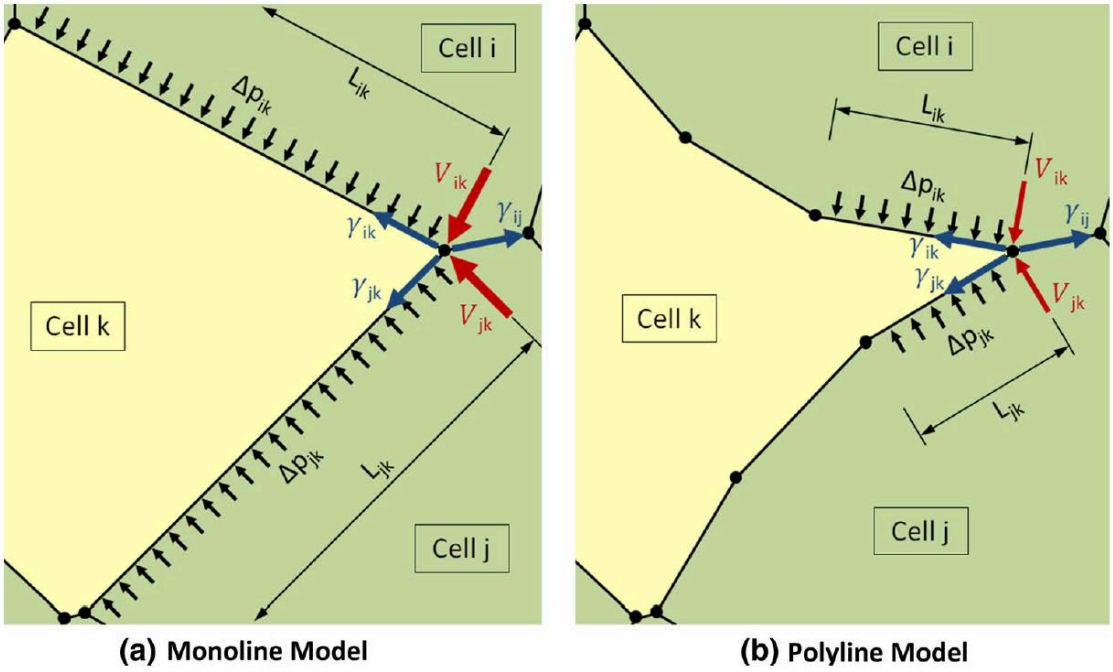

Figure 16. How Monoline Model Restricts Motion
(Perrone et al., 2015)

The edge tensions in the figure were chosen so that they should pull the yellow cell between the two green cells. The lengths of the tension vectors do not reflect their relative magnitudes. When cell edges are forced to remain straight, as in (**a**), intracellular pressure differences may act over a long enough length that the equivalent shear forces transmitted to the triple junction (in this case between cells *i*, *j* and *k*) can prematurely arrest its motion. When a polyline model is used (**b**), the segment lengths are shorter and the resulting shear forces have a much reduced effect. Caption from (Perrone et al., 2015).

To motivate the study, the interfacial tensions γ in Figure 16 were selected to make the yellow cell draw between the two green cells and the polyline model was successful (Figure 16B). However, the elevated shear loads V_{jk} associated with the monoline model's substantially longer edges L_{jk} are sufficient to counteract the triple junction tension imbalances, blocking further rightward motion of the triple junction between cells i, j, and k, and obstructing invasion of the yellow cell. This motivating example demonstrates another effect of a

polyline model: the intermediate nodes displace laterally with respect to the boundary. They move until the tensions along adjacent segments form an angle at which the transverse components of the edge tensions just balance the pressure forces, like a discretized membrane (Perrone et al., 2015). The results of the study will be reported in the next chapter.

A 'tear-drop' shape and F-actin enrichment in a single anterior protrusion and in the cell posterior characterize cells intercalating to the basal surface (Neumann et al., In Submission). CellFIT-3D will be used to determine if increased interfacial tensions correlate with enriched F-actin. However, anterior protrusions and posteriorly increasing tension gradient must be modelled to test their sufficiency to elongate mammary epithelium.

Anterior protrusions were incorporated into the monoline and polyline models by manipulating the Brodland lamellipodium model (Brodland, 2006; Brodland & Veldhuis, 2006). When a protrusion extends from cell i and fills the interface between cells j and k (Figure 17A), the original interfacial tension strength γ_1 is replaced with a specified protrusive tension strength γ_2. If the protrusive tension strength is strong enough, the interface between cells j and k will shorten and cell i will intercalate between cells j and k according to the neighbour change algorithm described earlier. A new protrusion will extend along a new interface and the process will start again. Giving the cell a migration direction can specify the interface in which the protrusion extends along (Neumann et al., In Submission). For example, the protrusion of cell i extends from left to right along the interface closest to being parallel to horizontal axis.

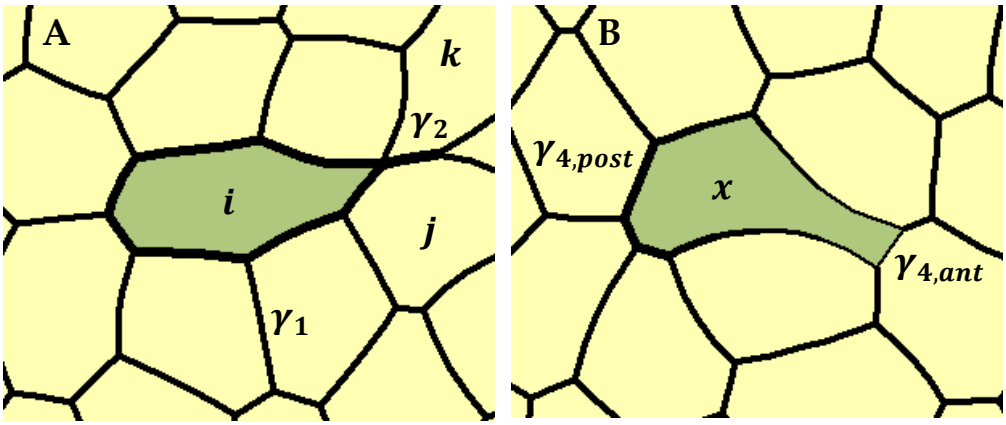

Figure 17. Anterior Protrusion and Posterior Tension Gradient Schematic
(**A**) FE model cell i intercalating between cells j and k with an anterior protrusion of tension strength γ_2 as opposed to the field tension strength γ_1. (**B**) FE model cell x with posteriorly increasing tension gradient. The circumferential tension linearly varies from an anterior minimum $\gamma_{4,ant}$ to a posterior maximum $\gamma_{4,post}$.

Posteriorly increasing tension gradients were modeled by specifying the minimum anterior tension $\gamma_{4,ant}$, the maximum posterior tension $\gamma_{4,post}$, and linearly varying the circumferential tension between those values (Figure 17B). The line thickness in Figure 17 represents the relative interfacial tension strength. Similar to the anterior protrusion model, the axis defining the direction of the tension gradient may be specified. For example, cell x in Figure 17B has been specified to migrate from left to right. Therefore, cell x has high posterior tension on the left side and low anterior tension on the right side.

4. Monoline vs Polyline Study

This chapter consists of work paraphrased from a published paper (Perrone et al., 2015). The discrepancies between monoline and polyline models were investigated by considering a wide variety of common cell-cell interaction, including annealing, single- and multi-cell engulfment, sorting, and two forms of mixing (invasion and checkerboard pattern formation). These phenomena are key building blocks for embryogenesis and wound healing.

4.1 Annealing

An isolated group of cells of a single type were formed from a Voronoi tessellation (H. H. Chen & Brodland, 2000). All cell interfaces were assumed to produce the same edge tension γ in accordance with equations like those for a pressure vessel (Boal, 2012; Brodland et al., 2007). The cell size was varied to produce pressure differences between neighbouring cells (Table 1, Row A). Both the monoline and polyline models proceeded until they produced equilibrium topologies in which all meaningful motion had stopped (last two columns of Table 1). The models produced similar topologies; however, the polyline model was able to produce cell shapes consistent with those seen in Figure 15 and other published studies (Eisenhoffer et al., 2012; Maitre et al., 2012; Solon, Kaya-Copur, Colombelli, & Brunner, 2009). The longer exterior interfaces displayed higher curvature than the short interior interfaces by spacing the intermediate nodes according to polyline segment length (Perrone et al., 2015). The resulting pressures in the smaller cells were higher than those in the larger cells and the pressure differential produced bulging interfaces (Perrone et al., 2015). The curvature of each interface was proportional to the pressure difference across it,

as described by the Young-Laplace equation described earlier (Brodland et al., 2014).

Table 1. Comparison of Monoline and Polyline Model Simulations (Perrone et al., 2015)

	γ	Initial Configuration	Monoline Model Terminal Configuration	Polyline Model Terminal Configuration
A. Annealing	$\gamma = 10$			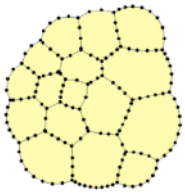
B. Cell Engulfment	$\gamma_{GY} = 20$ $\gamma_{GM} = 40$ $\gamma_{YM} = 70$	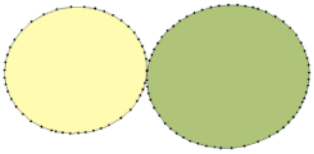	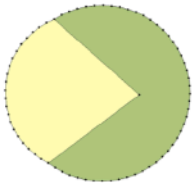	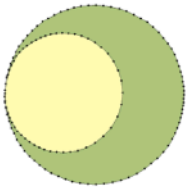
C. Tissue Engulfment	$\gamma_{GG} = 95$ $\gamma_{YY} = 40$ $\gamma_{GY} = 55$ $\gamma_{GM} = 80$ $\gamma_{YM} = 140$	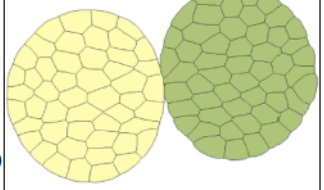	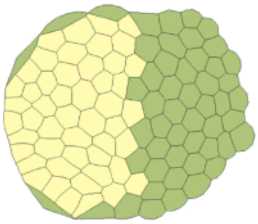	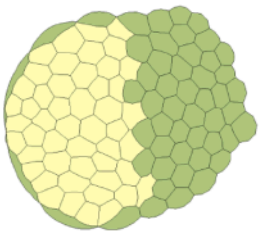
D. Sorting and Engulfment	$\gamma_{GG} = 10$ $\gamma_{YY} = 10$ $\gamma_{GY} = 40$ $\gamma_{GM} = 50$ $\gamma_{YM} = 100$	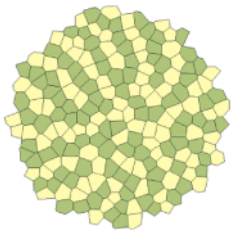	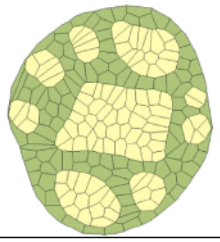	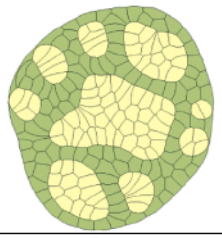
E. Invasion	$\gamma_{GG} = 20$ $\gamma_{YY} = 12$ $\gamma_{GY} = 10$ $\gamma_{GM} = 20$ $\gamma_{YM} = 20$	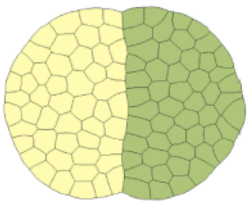	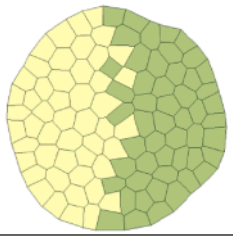	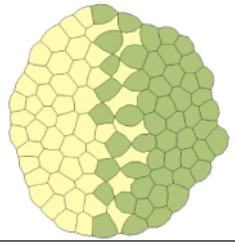
F. Checkerboard	$\gamma_{GG} = 20$ $\gamma_{YY} = 20$ $\gamma_{GY} = 10$ $\gamma_{GM} = 20$ $\gamma_{YM} = 20$	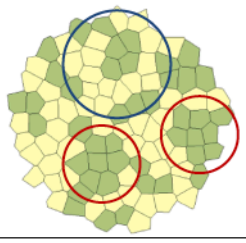	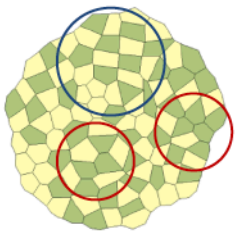	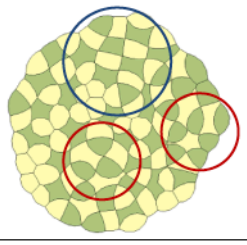

The title of each scenario is shown in the first column of the table, and the surface and interfacial tensions used for each are reported in the second column. The middle column gives the initial configuration for both models, and the terminal states (the geometries at which further meaningful movement ceases) for the monoline and polyline models are shown in the second last and last columns, respectively. Caption from (Perrone et al., 2015).

RMS errors between the angles produced by the models and the corresponding theoretical Young angles (Davies & Rideal, 1963) were calculated for each triple junction. The monoline model angle errors were distributed uniformly from 2.5° to 40°, with a mean of 19.5° and a median of 20.7° (Perrone et al., 2015). These errors may not significantly affect the appearance of the angles; however, they complicate edge force calculations (Viens, 2006) and force inference methods (Brodland et al., 2014), as previously discussed. The polyline model angle errors ranged from 0.04° to 2.8° with one outlier at 9.0°, had an average RMS error of 1.2°, and had a median value was 0.69° when circular arcs were fit to the multiple points along each interface (Brodland et al., 2014). The polyline model angle errors were sufficiently small for the successful application of force inference methods (Brodland et al., 2014).

A discrepancy percentage was calculated for angle error, boundary length, and cell displacement (Figure 18). The reported discrepancy percentages were equal to the difference in the monoline and polyline values divided by their mean and integrated over time (Perrone et al., 2015). The reported curvature values were those of a particular interface in the polyline model at the terminal configuration because the monoline model produced only zero values (Perrone et al., 2015). In the annealing study, the internal interface curvatures of the polyline model were small and little difference was seen between the two models (Perrone et al., 2015). The total interface length of a specific kind and the average distance

between the initial and final locations of the cell centroids were reported as the boundary length and displacement discrepancies, respectfully (Perrone et al., 2015). Neither measure revealed meaningful model differences for the annealing study (Perrone et al., 2015).

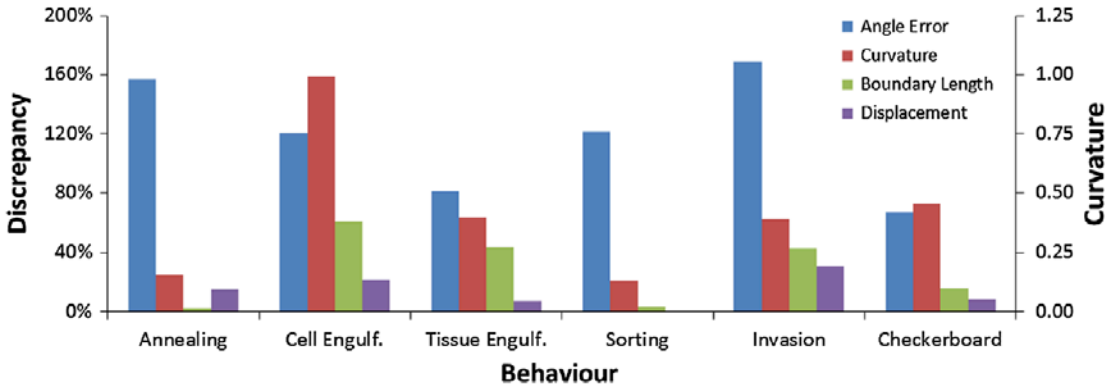

Figure 18. Quantitative Comparison of Monoline and Polyline Models (Perrone et al., 2015)

The models are compared in terms of angle error, curvature, boundary length and displacement for each cell interaction scenario. Details of the calculations are given in the text and may vary from one scenario to the next, depending on the particular features of interest. All values are reported as percentage differences between the monoline and polyline models (*left ordinate*), except for curvature (*right ordinate*). Caption from (Perrone et al., 2015).

4.2 Cell Engulfment

Two cells coloured yellow and green to represent different type (Brodland, 2004) were placed side by side (Row B of Table 1) and prescribed interfacial tensions such that the green cell should totally engulf the yellow cell (Brodland, 2002). Phagocytes completely engulf apoptotic cells (Ravichandran & Lorenz, 2007) and bone cells partially or completely engulf coated beads applied to orthopaedic implants during osseointegration (Tache, Gan, Deporter, & Pilliar, 2004). The tension along the yellow-medium interface must be greater than the sum of the

tensions along the green-medium and green-yellow interfaces to pull the green cell over the surface of the yellow cell (Brodland, 2002).

The monoline model produced partial engulfment and unrealistic cell shapes (Row B of Table 1). The virtual shear forces associated with modelling intercellular edges as beams restrained motion at the triple junctions along the aggregate perimeter (Perrone et al., 2015). However, the virtual shear forces were significantly smaller and the intracellular yellow-green interface wrapped around the yellow cell, formed a crescent shape and produced complete engulfment, when it was modelled as a polyline (Row B of Table 1). Figure 18 reports the discrepancy measures for angle error of the triple junctions along the aggregate perimeter, yellow-medium interface length, centroid displacement of the green cell, and curvature of the yellow-green interface.

4.3 Tissue Engulfment

The cell engulfment study was extended to tissue engulfment, an extensively studied phenomenon (Armstrong, 1989; Foty, Pfleger, Forgacs, & Steinberg, 1996; Phillips & Steinberg, 1978; Steinberg, 1963; Steinberg, 1962; Steinberg, 1970). Two tissues of different type were placed adjacent to each other and interfacial tensions were prescribed for the green tissue to completely engulf the yellow aggregate (Row C of Table 1). The cell-medium and heterotypic interfacial tension requirements for tissue engulfment are similar to those of cell engulfment with an additional requirement. The tensions present along the green-green interfaces must be sufficiently high to shorten the interface and allow green cells to be drawn away from the green tissue and flow over the surface of the yellow tissue (Perrone et al., 2015). However, the green-green interfacial tension must be

bounded to prevent pulling yellow cells between greens cells at the heterotypic interface (Perrone et al., 2015). The additional neighbour change embargo timer was used in this study because new edges along the yellow-medium interface were quickly shortening and triggering a new neighbour change that undid the one that just happened (Perrone et al., 2015). This was a result of the large difference between the tension acting along the yellow-medium interface and those of the surrounding interfaces (Perrone et al., 2015).

The monoline model produced partial engulfment while the polyline model demonstrated complete engulfment (Perrone et al., 2015). The difference between the models was caused by the engulfing cells in the polyline model better separating from the original tissue and stretching further around the engulfed tissue (Perrone et al., 2015). Three green cells dissociated from the bottom edge of the green tissue and formed a string of engulfing cells in the polyline model, while only two dissociated in the same region of the monoline model (Perrone et al., 2015). The next cell that would have dissociated was restrained from doing so by its shape constraints. The discrepancy values shown in Figure 18 report angle error for all triple junctions, the boundary length of the yellow-medium interface, centroidal displacements of the green cells on the heterotypic interface, and curvature of the heterotypic interface (Perrone et al., 2015).

4.4 Sorting and Engulfment

Two hundred cells of two types were arranged into an aggregate (Row D of Table 1) and prescribed interfacial tensions to produce sorting and engulfment (Brodland, 2002). Embryonic cells in heterotypic aggregates can spontaneously sort by type (Foty et al., 1996; Glazier & Graner, 1993; Harris, 1976; Hutson,

Brodland, Yang, & Viens, 2008; Krens & Heisenberg, 2011; Moscona, 1952; Moscona, 1957; Steinberg, 1963; Townes & Holtfreter, 1955). Sorting and engulfment must be considered together when studying finite aggregates that contact the medium (Armstrong, 1989; Brodland, 2002).

The terminal states of both models (Row D of Table 1) are similar in terms of the number, sizes, and shapes of the homotypic islands produced (Perrone et al., 2015). Furthermore, compact and simple cells shapes are found in both models, suggesting that complex shapes are not required for this phenomenon (Perrone et al., 2015). Figure 19 presents the relationship between the evaluation criteria and dimensionless time. The median angle error in the polyline model reduces from approximately one-third to one-seventh of the monoline value over the duration of the simulation (Figure 19a). The mean curvature along the heterotypic cell–cell interfaces of the polyline model is relatively constant (Figure 19b). The total heterotypic interface length decreases in a similar manner for the two models (Figure 19c); however, the polyline length decreases slightly more quickly, which may be a result of its cells being more compliant (Perrone et al., 2015). Cells along the heterotypic boundary moved to a similar extent in the models (Figure 19d).

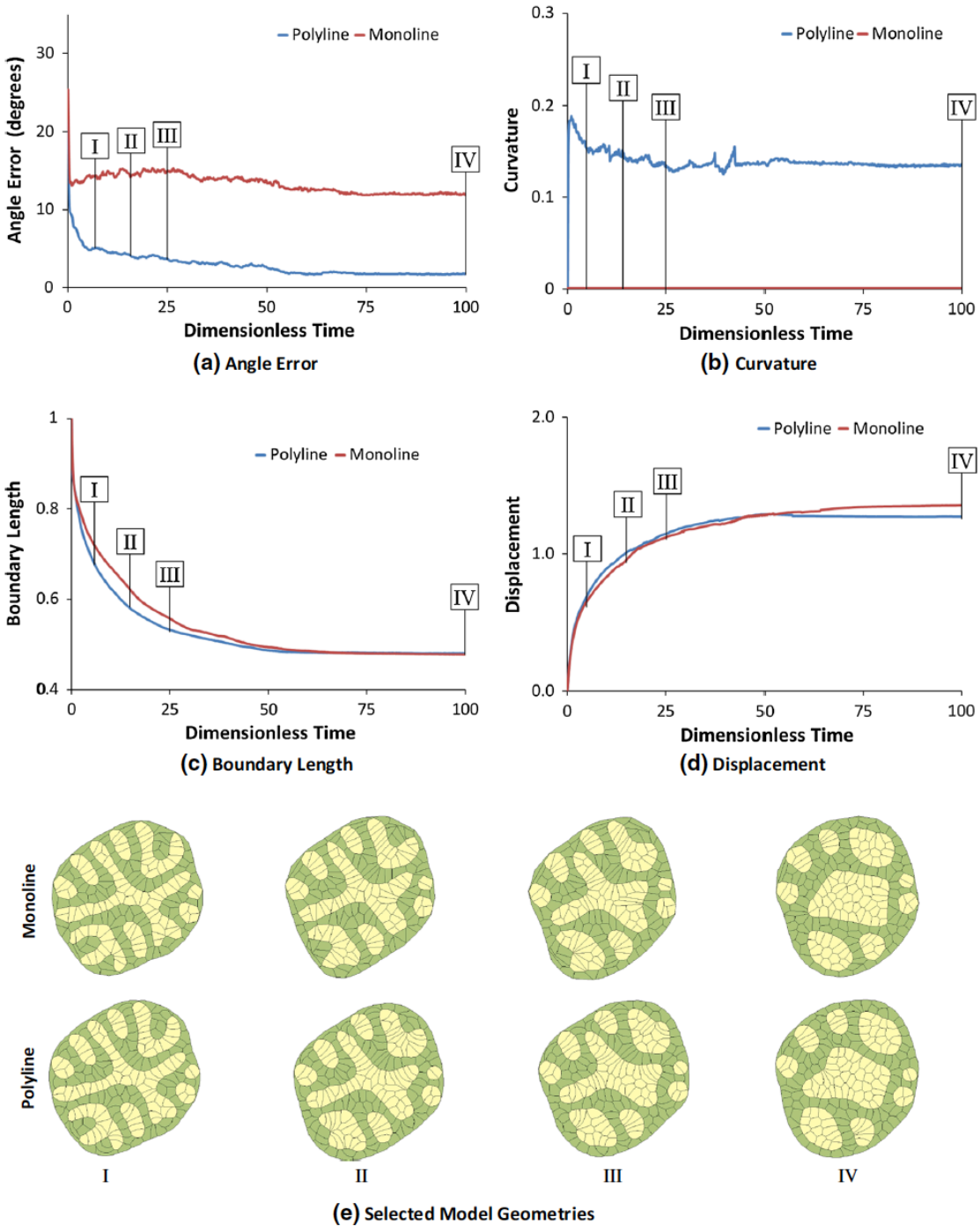

Figure 19. Detailed Cell Sorting and Engulfment Comparison (Perrone et al., 2015)

(a) Relationship between RMS angle error (see text for details) and dimensionless time. (**b**) The average absolute value of edge curvature normalized to a circle of the same area as the average cell. (**c**) The total length of the yellow–green boundary normalized to its initial length. (**d**) Displacement (see text for details) normalized to cell diameter. (**e**) The geometries of the

aggregates corresponding to the Roman numerals on the graphs. Caption from (Perrone et al., 2015).

4.5 Invasion

An aggregate of cells was divided into two cell types (Row E of Table 1) and the interfacial tensions in this study were set such that single cells from one homotypic group (yellow) partially or completely leave that group and mingle with cells of another type (green), known as invasion (Brodland, 2002). The interface between mesenchymal and myocardial tissues of a developing avian heart is dispersed as a result of invasion along their common border (Armstrong & Armstrong, 1990). Epithelial and endothelial cells behave invasively during wound healing (Brugues et al., 2014) and angiogenesis (Armstrong & Armstrong, 2000), respectively. Invasion is a complex mechanical phenomenon involving interactions between the invading cell and its neighbouring cells (Perrone et al., 2015). The green-green interfaces have relatively high tensions compared to those of the yellow-yellow and yellow-green interfaces to shorten and pull adjacent yellow cells in between green cells (Perrone et al., 2015).

Figure 18 quantifies the discrepancies between the models and Figure 20 provides temporal data. Figure 20a shows the polyline angle errors were smaller than those of the monoline model. The more complex shapes of the invading yellow polyline model cells (Row E of Table 1) were quantified by measuring the green-yellow interface curvature (Figure 20b). The curvature measure indicates that the polyline model deformed in a mode different from that of the monoline model cells (Perrone et al., 2015). The yellow cells of the polyline model invaded substantially further into the green cells than their monoline counterparts (Row E of Table 1). This discrepancy was quantified by measuring the length of the

yellow-green interface (Figure 20c) and by measuring the centroidal displacement of the invading yellow cells (Figure 20d). The virtual shear forces associated with modelling cell edges as beams likely induced the observed motion restraint of the monoline model. Interestingly, when the monoline geometry at dimensionless time 100 is converted into a polyline model (dashed red curve), angle error (Figure 20a), yellow–green interface curvature (Figure 20b), yellow–green interface length (Figure 20c), and the displacements of cells that began at that interface (Figure 20d) approach those of the polyline model (Perrone et al., 2015).

The yellow cells stop invading once they are completely surrounded by green cells because the forces driving them forward now equal the forces pulling them backward (Perrone et al., 2015). Additional mechanisms that prevent equilibrium must come into play for cells to move more than one cell diameter, or two diameters if cell positional exchanges occur, as in this case (Perrone et al., 2015).

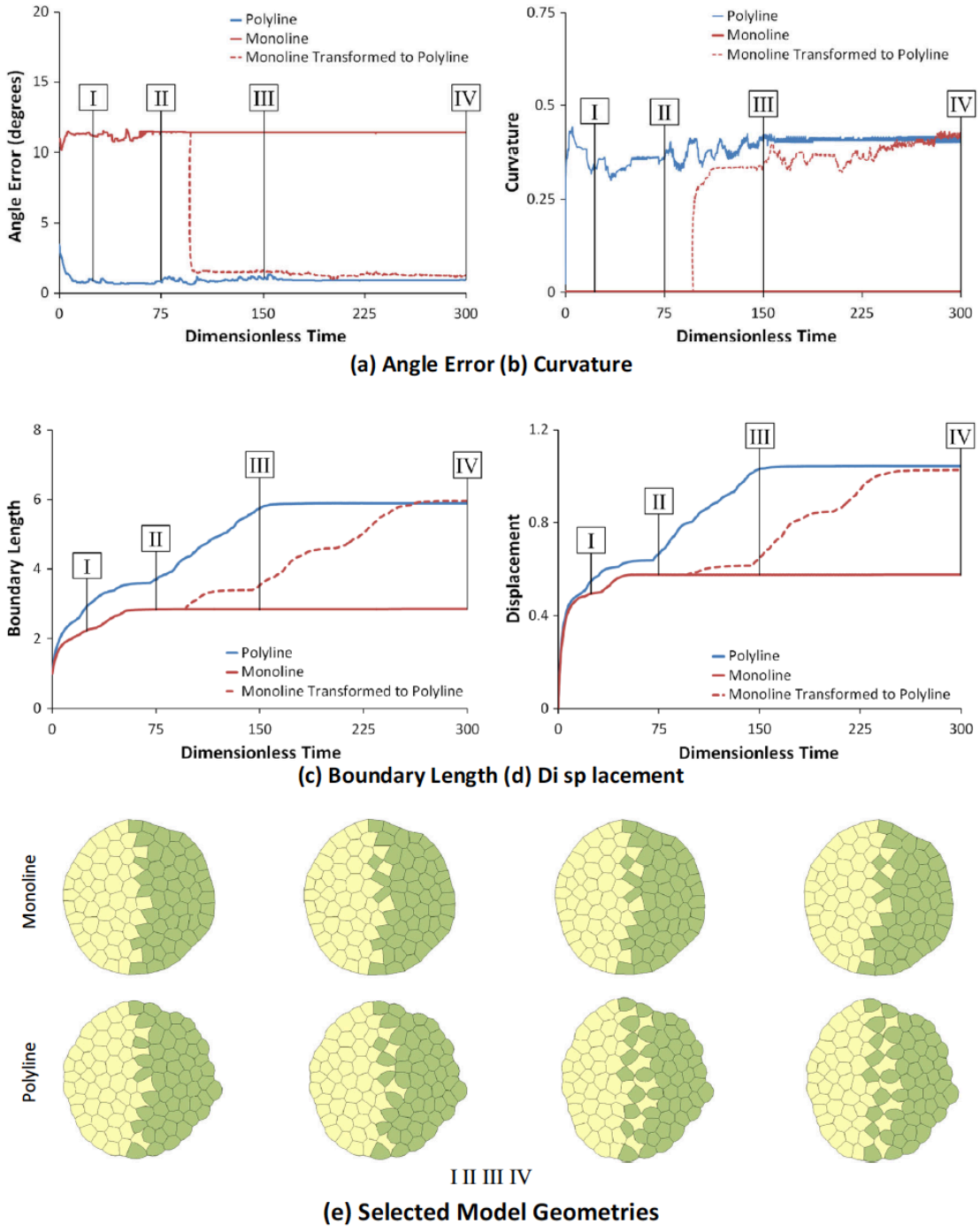

Figure 20. Detailed Invasion Comparison
(Perrone et al., 2015)

(a) Relationship between RMS angle error (see text for details) and dimensionless time. (**b)** The average absolute value of edge curvature normalized to a circle of the same area as the average cell. (**c**) The total length of the yellow–green boundary normalized to its initial length. (**d)** Displacement (see text for details) normalized to cell diameter. (**e**) The geometries of the

aggregates corresponding to the Roman numerals on the graphs. Caption from (Perrone et al., 2015).

4.6 Checkerboard Patterning

Finally, a heterotypic aggregate of two cell types were prescribed interfacial tensions to produce checkerboard patterns (Row F of Table 1). The formation of checkerboard patterns is less common than invasion because heterotypic interfaces are favoured over both homotypic ones. Considered to be an extreme case of cell mixing, it does occur on the luminal surface of adult Japanese quail. The oviduct epithelium is a monolayer sheet of ciliated cells and gland cells. These two cell types assemble into a checkerboard-like pattern from a star-like one during sexual maturation (Honda, Yamanaka, & Eguchi, 1986).

The models produced similar results in terms of cell locations and overall degree of checkerboard patterning (Perrone et al., 2015). Figure 18 shows discrepancy between the monoline and polyline model angle estimates; however, it is smaller than the other studies. The degree of checkerboard patterning in the homotypic green regions is the distinguished difference between the models. The blue circle (Row F of Table 1) outlines an area where both models produced similar results, while the red circles indicate areas where the polyline model outperforms its monoline counterpart (Perrone et al., 2015). The monoline model failed to reproduce the significant curvatures that arise along the heterotypic boundaries of the polyline model (Row F of Table 1 and Figure 18). The monoline model is restrained because it lacks the required shape compliance (Perrone et al., 2015). However, the monoline model adequately reproduced the heterotypic boundary length and centroid displacements generated by the polyline model (Figure 18).

5. Branching Morphogenesis Study

This chapter consist of work paraphrased from a paper that has been submitted for publication (Neumann et al., In Submission). The interfacial tensions associated with the proposed molecular activities and cellular behaviour responsible for driving epithelial tube morphogenesis were determined. Then, FE modeling was used to test the sufficiency of the associated interfacial tensions to drive epithelial tube morphogenesis. Finally, a prediction model was proposed in which cell motility behaviour may be predicted solely by force inference.

5.1 3D Force Inference

The interfacial tensions associated with cell migration and intercalation were determined using CellFIT-3D (Veldhuis et al., 2017). Meshes defining the shapes and intersections of the cell membranes were constructed from geometrical information extracted from 3D confocal images (Figure 21A). The angles between cellular junctions were calculated (Figure 21B) and used to generate Young's equations, which were solved to determine relative interfacial tension values. This method was applied to the phenotypic cell shapes for migration, intercalation, and columnar organization (Figure 21C-E). Both migrating and intercalating cells displaying the 'tear-drop' shape phenotype were found to have high tension in anterior protrusions and a gradient of circumferential tension which increased towards the cell posterior (Figure 21C,D). Recall that the biosensor imaging had revealed F-actin accumulation in both regions. The high anterior protrusion tension causes the sides of the cell to frame to a narrow anterior and the posteriorly increasing tension causes the posterior of the cell to become curved into a 'tear-drop' shape. Cells that successfully intercalated to the basal surface were observed to transition to non-motile columnar cells. These

cells no longer displayed high anterior protrusion tension or posterior tension gradients, but displayed relatively low tension laterally and intermediate tension anteriorly and posteriorly (Figure #E). The relatively higher anterior and posterior tensions cause the anterior and posterior of the cell to shorten and the sides of the cell to lengthen into a columnar shape (Neumann et al., In Submission).

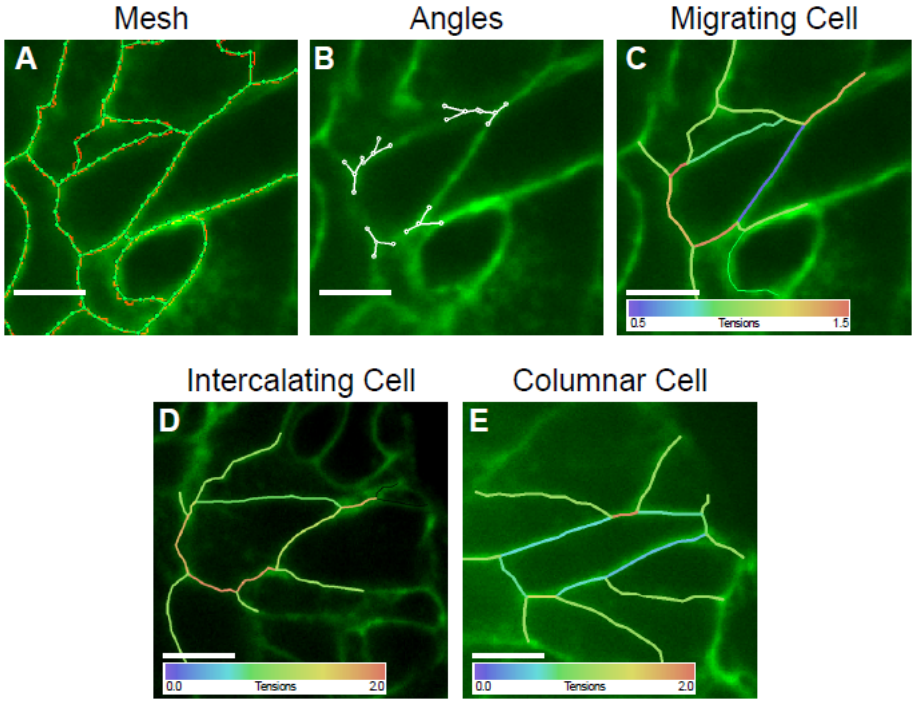

Figure 21. CellFIT-3D Applied to Key Cell Phenotypes
(Neumann et al., In Submission)

(**A**) CellFIT-3D was applied to confocal z-stacks of membrane labeled organoids (tdTomato, green) to generate a mesh. Membranes were segmented using a watershed filter to reconstruct 3D cell shape. CellFIT-3D segments (green) are shown overlaid on a cell of interest. Scale = 5 μm. (**B**) Curvilinear triple junctions (where three cells meet) were reconstructed using vectors to define the relative angles between them. Six triple junction vector diagrams (gray) are shown on a cell of interest. (**C**) Migrating cells often display a 'tear-drop' shape. CellFIT-3D analysis revealed high interfacial tension in the anterior protrusion and a gradient of tension increasing towards the posterior. Relative tension scale: low (violet) to high (red). (**D**) Intercalating cells also exhibit high interfacial tension in the anterior protrusion and a gradient of tension increasing towards the posterior. Relative tension scale: low (violet) to high (red). (**E**) Columnar epithelial cells display modestly higher anterior and posterior tensions, relative to lateral tensions. Relative tension scale: low (violet) to high (red). Caption from (Neumann et al., In Submission).

5.2 2D Finite Element Migration Model

The force inference analysis revealed anterior protrusions and posterior tension gradients to be potential physical mechanisms for migration. A 2D FE model of epithelial cells migrating within a tissue was constructed to test the sufficiency of the potential mechanisms to generate migration and distinguish their relative advantages and disadvantages. A tissue of cells was generated from a Voronoi tessellation (H. H. Chen & Brodland, 2000) in which interfacial tensions were prescribed to vary by up to ±15% in a random fashion. 5 cells were randomly selected to possess an extending anterior protrusion with a 1.5x tension strength relative to the field tension (green cells; Figure 22A). The cells migrated successfully past neighbouring cells, revealing that protrusions were sufficient. Next, migration based solely on a posterior tension gradient was tested. The same 5 cells used in the protrusion migration study were given an increasing gradient of interfacial tension from 0.5x anterior to 1.5x posterior tension strength relative to the field tension (green cells; Figure 22B). The cells also migrated successfully, revealing that posterior tension gradients were sufficient. However, the corresponding cell shapes were not observed experimentally and the two mechanisms were considered to act in combination (Neumann et al., In Submission). The contribution of each mechanism was yet to be determined.

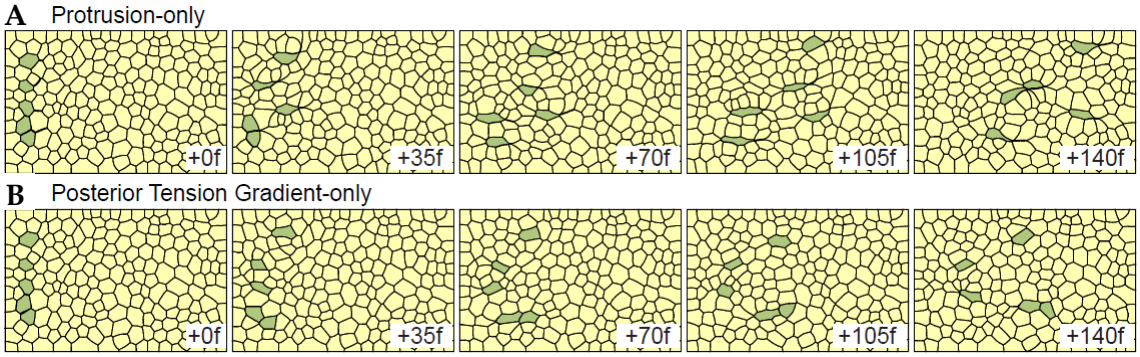

Figure 22. 2D Finite Element Migration Model
(Neumann et al., In Submission)

(**A**) Five cells were selected to randomly extend rightward anterior protrusions at 1.5x tension strength relative to field tension. Cells migrated successfully. Line width indicates relative tension strength. (**B**) Five cells were selected to randomly generate a posterior tension gradient of 0.5-1.5x tension strength relative to field tension. Cells migrated successfully. Line width indicates relative tension strength. Caption from (Neumann et al., In Submission).

5.3 2D Finite Element Terminal End Bud Model

Having identified two potential mechanisms of migration within a tissue, the model was then extended to include the spatial constraints of intercalating to a boundary, as was shown to be the case with branching morphogenesis. A tissue of cells with no horizontal constraints and high basal tension (dark line, top of dark green cells, Figure 23A) was generated. Cells touching the basal surface were encoded dark green and interior cells were encoded light green. The interfacial tension along the basal surface was set to 1.5x field tension to give a smooth surface, as was observed in elongating branches in culture and *in vivo* (Ewald et al., 2008). Interior cells (light green) were randomly selected to both protrude (e.g. blue cell, Figure 23A" +1f, black arrow) and have a posterior tension gradient (Figure 23S", +1f, blue arrowhead). These changes were sufficient to induce intercalations (Figure 23A"). Some intercalating cells did not extend to the basal surface and regressed into the tissue interior. If an intercalating cell extended to the basal surface, a time-varying mechanism was

triggered to expand the basal surface via decreased anterior and increased posterior tensions (Figure 23A″, +3-4f) and establish stable boundary capture via decreased posterior and increased anterior tensions (Figure 23A″, +12f). Intercalations across the tissue were sufficient to reduce the number of cell layers and increase the length of the tissue (Figure 23A′).

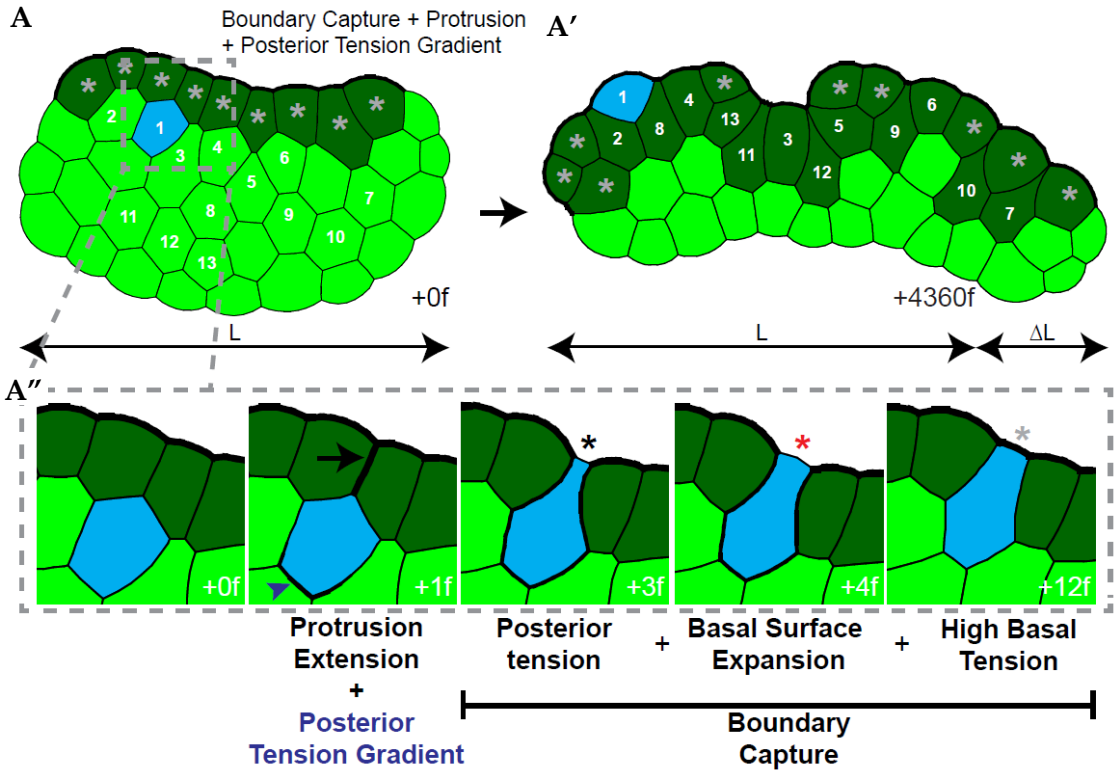

Figure 23. 2D Finite Element Boundary Capture Model
(Neumann et al., In Submission)

(**A**) A FE model was generated of a tissue with high basal surface tension (dark green cells) to test candidate intercalation mechanisms. Cells were randomly chosen to intercalate towards the basal surface using high anterior protrusion tension and a posterior tension gradient. (**A′**) The combined intercalation mechanism was sufficient for elongation. (**A″**) Intercalating cells generated an anterior protrusion (black arrow) and a posterior tension gradient (blue arrowhead) towards the basal high tension line (+1f). Cells were captured at the basal surface through a combination of posterior tension and focal disruption of the high basal tissue tension (+3f, black star). The basal surface of the intercalating cell then expanded (+4f, red star). Intercalation was made permanent when high basal tension was restored (+12f, light gray star). Line width indicates relative tension strength. Caption from (Neumann et al., In Submission).

Having established that the combined mechanism of protrusion extension, posterior tension gradient, and boundary capture was sufficient for intercalation, the tissue of cells was wrapped around a lumen to generate a 2D model depicting a section through a 3D TEB (Figure 24A). Cells touching the basal surface were encoded dark green and interior cells encoded yellow were capable of proliferation, migration, and intercalation. The same iterative program of specified protrusion strengths (P), specified posterior tension gradients (T), and boundary capture (Bc) was applied to the model. However, the *in silico* TEB did not elongate and instead formed clusters of small buds (Figure 24A″). This disorganized morphology is in contrast with the smooth basal surface that was observed along elongating branches in culture and *in vivo* (Ewald et al., 2008).

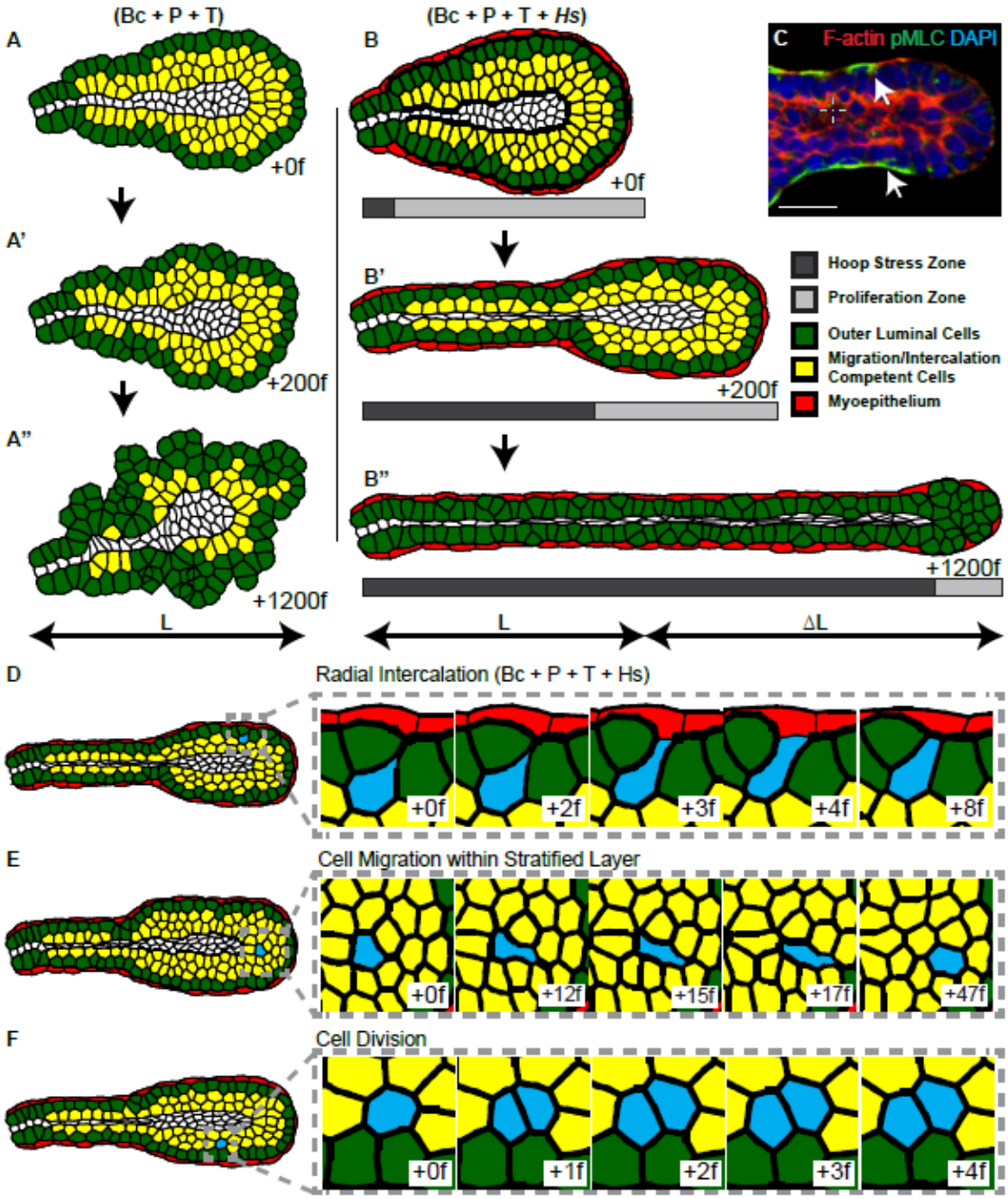

Figure 24. 2D Finite Element Terminal End Bud
(Neumann et al., In Submission)

(**A**) A FE model of a terminal end (TEB) was generated to test the combination of anterior protrusion (P), posterior tension gradient (T), and boundary capture (Bc) driven intercalation. Interiors cells could migrate and divide and a subset were randomly chosen to intercalate (yellow), with random protrusion and tension gradient strengths, directed towards the basal most luminal cell layer (green cells). The lumen does not affect cellular tensions. These mechanisms resulted in disorganized growth and did not efficiently elongate the tissue. (**B**) The

FE model from (**A**) was extended to include high basal tension and in-plane stress applied towards the organoid center-line (hoop stress), to model the function of the contractile myoepithelium (red). The region in which the hoop stress (dark gray) was applied or cell proliferation (light gray) occurred varied over time (**B'** and **B"**). The combination of anterior protrusions (P), posterior tension gradients (T), boundary capture (Bc), and high basal hoop stress (Hs) was sufficient to drive tissue elongation. (**C**) A confocal image of an organoid branch showing F-actin (red), phospho-Myosin Light Chain (pMLC, green), and nuclei (DAPI, blue). Scale = 20 μm. Representative of staining in 49 orgs, r=3. (**D**) An interior cell (blue) intercalating via the mechanisms identified in (**B**). (**E**) An interior cell (blue) migrating in the tissue via the mechanisms identified in (**B**). (**F**) An example of cell proliferation (blue) in the stratified region. Caption from (Neumann et al., In Submission).

A smooth boundary surface corresponds to high tension acting along the boundary. Therefore, phospho-myosin light chain (pMLC), a marker for actin dynamics (Ewald et al., 2008), was used and was found to be concentrated at the trailing duct and typically undetectable at the front of the TEB (Figure 24C). The 2D basal boundary in the model represents the edge of a 3D cylinder. A smooth cylindrical surface would correspond to high tension in both the axial and circumferential directions. To model the 3D myoepithelial influence in 2D, an effective circumferential hoop stress (Figure 24B, red cell layer) and basal tension (Figure 24B, thick basal line) were added to the model. Interior cells (yellow) in the stratified layer were capable of radial intercalation (Figure 24D, blue cell), migration (Figure 24E, blue cell), and cell division (Figure 24F, blue cells, corresponding to Figure 24B-B", Proliferation Zone, light gray). The effective hoop stress in the model concurrently moved along with the duct as it elongated (Figure 24B-B", Hoop Stress Zone, dark gray). The effective hoop stress and basal tension additions enabled the *in silico* TEB to elongate and resolve to a bilayer, while maintaining plausible cell and tissue morphologies (Figure 24B vs. 24A).

As an aside, the sufficiency of anterior protrusions or posterior tension gradients to drive intercalation within the *in silico* TEB, without the boundary capture

mechanism, was tested. Separate models were created in which interfacial tensions randomly varied and randomly selected cells generated either protrusions or posterior tension gradients, but not both. Protrusive cells intercalated to contact the basal surface but could not stabilize their position (Figure 25A, blue cell). Similar transient intercalations were experimentally observed, in which cells eventually retracted their protrusions and regressed to the tissue interior. Posterior tension gradient-only cells also transiently intercalated to the basal surface (Figure 25B, blue cell). In addition to the localized failure of intercalation, neither mechanism was sufficient to elongate the *in silico* TEB (Neumann et al., In Submission).

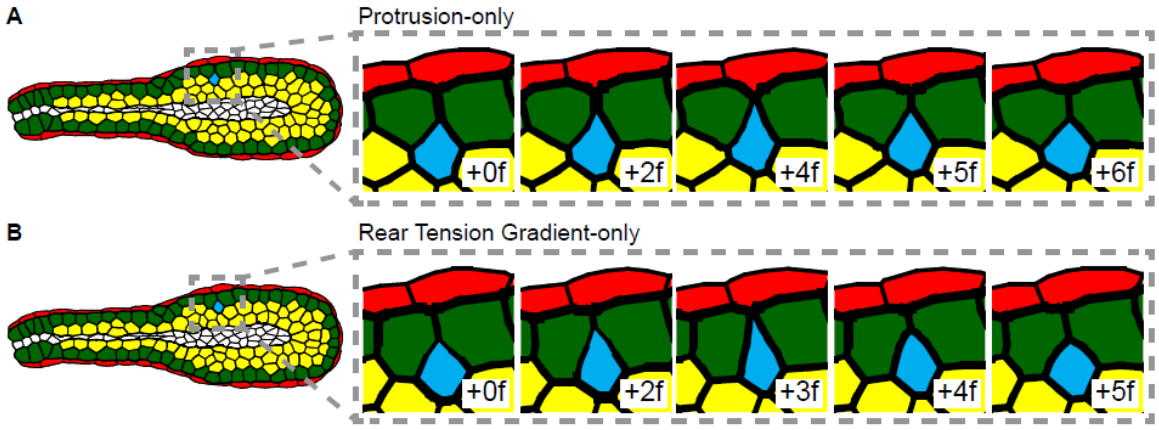

Figure 25. 2D Finite Element Model of Transient Intercalation (Neumann et al., In Submission)

(A) A FE model of a terminal end bud (TEB) was generated to test intercalation success using only anterior protrusion or posterior tension gradient. Interiors cells could migrate and divide and a subset were randomly chosen to intercalate (blue), with random protrusion and tension gradient strengths, directed towards the basal most luminal cell layer (green cells). The model also included high basal tension and in-plane stress applied towards the organoid center-line (hoop stress), to model the function of the contractile myoepithelium (red). The lumen does not affect cellular tensions. This mechanism resulted in no intercalation and did not efficiently elongate the tissue. **(B)** Posterior tension gradient-only intercalation. This mechanism resulted in no intercalation and did not efficiently elongate the tissue. Caption from (Neumann et al., In Submission).

5.4 Cell Migration and Intercalation Criteria

It was established that high tensions in anterior protrusions and along posterior surfaces were sufficient for cell migration but required a boundary capture mechanism during intercalation. Next, a parametric analysis of the relative contribution of pulling and pushing mechanisms was conducted. A cell must extend between cells at its anterior end and release from cells at its posterior end to successfully migrate inside a tissue. The anterior protrusion strength tension γ_2, circumferential tension strength γ_3, and the average field interfacial tension strength γ_1 are key parameters for protrusive migration (Figure 26A). Similarly, the minimum anterior tension strength $\gamma_{4,ant}$, maximum posterior tension strength $\gamma_{4,post}$, and the average field interfacial tension strength γ_1 are key parameters for posterior-tension-gradient migration (Figure 26B). The ratio between γ_2/γ_1 and $\gamma_{4,post}/\gamma_1$ was varied and applied to a single cell in the migration model. Success was defined as greater than 4-cell-lengths of migration (Figure 26C,E'). Unsuccessful cells were essentially immotile (Figure 26E). The analysis revealed that successful migration was defined by a sharp boundary (Figure 26C) and there was a range of effective modes, including protrusion-only (data point (1.8,1), Figure 26C), tension gradient-only mechanism (data point (1,1.5), Figure 26C), or combined mechanisms (intermediate data points, Figure 26C).

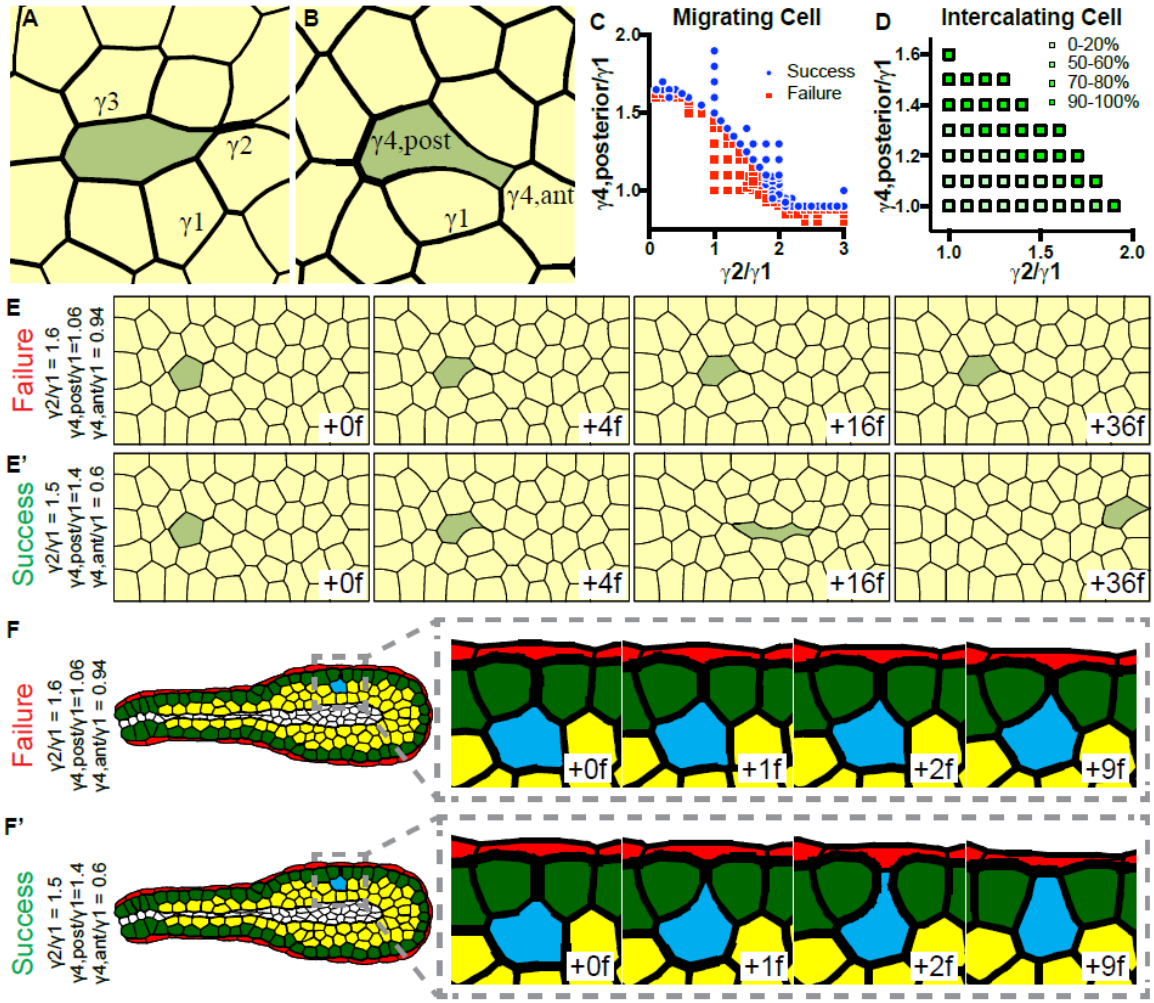

Figure 26. Relationship Between Cell Migration, Intercalation, and Interfacial Tension

(Neumann et al., In Submission)

(**A**) Characteristic shape of protrusion-only driven migration (green). γ_1 indicates the field tension magnitude, γ_2 indicates the anterior protrusion tension magnitude, and γ_3 indicates the circumferential interfacial tension magnitude. (**B**) Characteristic shape of posterior gradient-only driven migration (green). γ_1 indicates field tension magnitude, $\gamma_{4,post}$ indicates the maximum posterior tension magnitude, and $\gamma_{4,ant}$ indicates the minimum anterior tension magnitude. (**C**) Protrusion strength and gradient strength were varied across FEM simulations to define the mechanical characteristics of successfully migrating cells. Success was defined as ≥ four cell diameters. Tension magnitudes are defined as in (**A-B**). (**D**) Protrusion strength and gradient strength were varied across FEM simulations to define the mechanical characteristics of successfully intercalating cells, within the context of the TEB model from **24B**. Tension magnitudes are defined as in (**A-B**). Success is defined as persistent incorporation into the basal tissue surface. (**E**) Example of a failed cell migration (green). Protrusion and maximum gradient strengths are 1.6x and 1.06x field strength, respectively. (**E'**) Example of a successful cell migration (green). Protrusion and maximum gradient strengths are 1.5x and 1.4x field strength, respectively. (**F**) Example of a failed intercalation (blue), with protrusion strength of 1.6x and

posterior gradient strength of 1.06x field strength. (**F'**) Example of a successful intercalation (blue), with protrusion strength of 1.5x and posterior gradient strength of 1.4x field strength. Caption from (Neumann et al., In Submission).

The protrusion-only mode migrated by pulling through anterior cells and releasing from posterior cells, so long as protrusion strengths are greater than 1.9x field tension strength. The migrating cell anterior edges and the posterior edges of the cells being pulled on by the protrusion were concave and frame to a single point; creating a mirror effect (Figure 26A). The posterior tension gradient alleviated the pulling and releasing imbalance, and reduced the required protrusion strength to successfully migrate. Increasing the circumferential tension of the migrating cell (γ_3, Figure 26A) would also alleviate the pulling and releasing imbalance. The posterior tension gradient mode successfully migrated, so long as posterior gradient strengths were greater than 1.5x field tension strength. However, as mentioned earlier, the corresponding cell shapes were not observed experimentally. The migrating cell was pulled between anterior cells because of a reduction in anterior tension, and it released from posterior cells because of an increase in posterior tension. Different parameter combinations yield minor variations in shape. However, in general, successfully migrated cells displayed tear-drop shapes, with concave anterior edges framing to a single anterior protrusion and a round posterior (Neumann et al., In Submission).

Next, an analogous parametric analysis of intercalation within the *in silico* TEB was performed (Figure 26D). Unsuccessful cells did not reach the basal surface and receded into the tissue interior (Figure 26F), while successful cells reached the basal surface and stabilized their location, and remained at the basal surface (Figure 26F'). Intercalation success was characterized by the same criteria as

migration; the ability to pull between anterior cells is required to contact the basal surface and the ability to release from posterior cells is require to transition to a columnar cell. Intercalation differs from migration by the requirement of persistent incorporation into the basal surface; which is considered the third criteria. The criteria was met by the same migration modes, with slightly different protrusion and gradient strengths (Figure 26D), and the boundary capture mechanism previously described. Therefore, the physical features defining intercalation success are similar to those features defining migration success (Neumann et al., In Submission).

5.5 Predicting Cell Motility Behaviour

Four dimensional (three dimensions and time) images of branching morphogenesis were collected and ten cells were selected, five of which subsequently migrated (M) and five of which were non-motile (NM) during the observation window, to test the constructed motility criteria (Figure 26C-D). Blind to the outcome, CellFIT-3D was applied to a confocal stack of each cell at a single time point, the interfacial tension ratios were calculated, and motility predictions were generated by comparing the tension ratios to the criteria ratios. Seven of ten cells were correctly classified for motility based solely on their ratio of protrusion strength to posterior tension gradient at the single time point (concordant in green and discordant in red, Figure 27). Motile cells were indicated with an arrow marking the direction of their subsequent migration. The probability of achieving 7 or more of 10 binary choices correct, by chance, with 50% likelihood of each option is 17.2% by binomial theorem (Neumann et al., In Submission). This result, although too small of a sample size to definitively

say with confidence, suggests that motility behaviour may be predicted solely by determining the ratio of protrusion strength to posterior tension gradient.

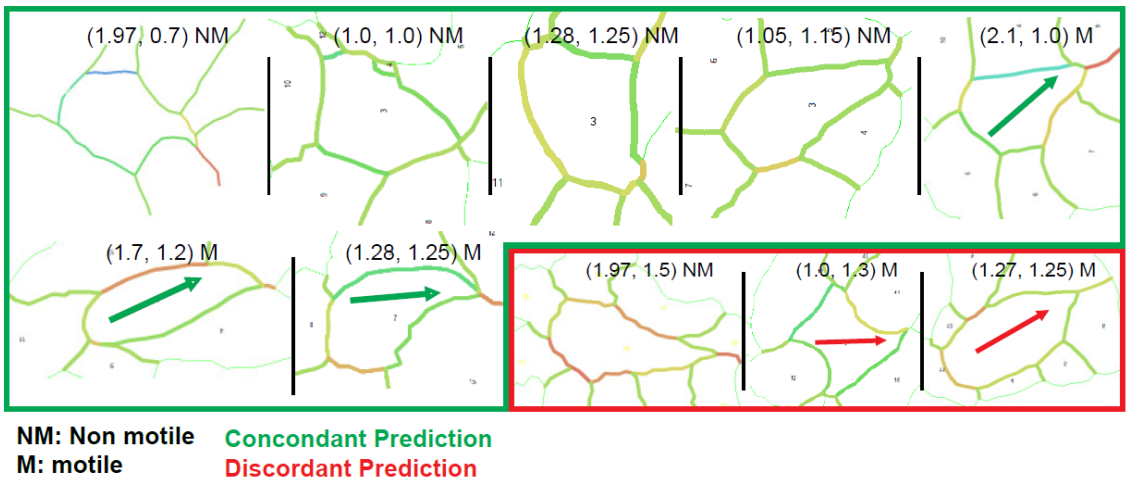

Figure 27. Cell Motility Behaviour Prediction Results
(Neumann et al., In Submission)

CellFIT-3D was used to define the relative strength of anterior protrusions and posterior tension gradients in 10 cells from elongating organoids. The criteria defined in (**26C**) were used to predict whether the cell would migrate. Blinded predictions correctly identified the migratory outcome in 7/10 cells. Caption from (Neumann et al., In Submission).

6. Discussion

Section 6.1 consists of work paraphrased from a published paper (Perrone et al., 2015). Section 6.2 of this chapter consists of work paraphrased from a paper that has been submitted for publication (Neumann et al., In Submission).

6.1 Monoline vs Polyline Study

The monoline versus polyline study showed that cells modeled with straight edges were subject to artificial shape constraints that may limit their ability to approximate triple junction angles, deformations, and motions. However, the cell shapes of the polyline models are less constrained like centric models (Brodland, 2004), while being entirely based on edge force mechanics. Therefore, polyline models combine the mechanical strength of finite element models, the curved-edge advantages of centric models, and the range of cell shapes available in Potts models (Perrone et al., 2015).

Significantly less angle error at triple junctions was produced by the polyline model than the monoline model (Figure 18). Checkerboard patterning and invasion were prone to producing relatively high numbers of groups of adjacent triple junctions representing quadruple and higher-order junctions, which attributed to higher degrees of angle error. Model enhancements that would allow higher-order junctions to be handled directly rather than being replaced with multiple adjacent triple junctions would improve angle reliability and further reduce overall angular error (Perrone et al., 2015).

The cell engulfment study illustrated the artificial shape constraint of the monoline model, as the ability of the cell surface to curve was vital to modeling

the behaviour (Table 1). Making the model cell edges polyline allowed the model to deform and move in a manner that conforms closer to the natural motions of the system, which is a fundamental principle in modelling (Zienkiewicz & Taylor, 2005). The monoline model was constrained by the monoline edges and was prevented from moving like the natural system. The polyline model can be trusted to be closer to the truth because it was able to undergo all of the motions of its simpler counterpart; another fundamental principle in modelling (Perrone et al., 2015). This study identified the range within which it is appropriate to use the monoline model (Brodland, 1988).

The polyline model was the more appropriate model for the tissue engulfment study because of its ability form more supple cell shapes, which resulted in more complete tissue engulfment (Row C of Table 1). However, it must be noted that the discrepancies between the two models were less in this scenario than in the cell engulfment study. The heterotypic boundary associated with tissue engulfment could be non-straight even though the edges of the cells from which they were formed may be straight because, as opposed to cell engulfment, the boundary involved multiple cells (Perrone et al., 2015).

The cell shapes of the polyline model in the invasion study provided important information that was not contained in the monoline model. The polyline model revealed easily identified shape differences between cell types. The model showed that when the green–green interfaces have elevated tensions, the yellow cells were drawn in and acquired distinctive star-like shapes, the kind of paradoxical findings that computational modeling is ideal for identifying (Figure 20E). Thus, the cell shapes indicated which cell type had the atypical properties

(the yellow ones, in this case). Consequently, polyline models must be used to model invasion because of the complex shapes that the invading cells acquire (Perrone et al., 2015).

This study suggests the monoline models may be suitable for modelling movements where cells remain largely isotropic in shape. The need for polyline models may not have been identified earlier because computational models focused on annealing, cell sorting, and checkerboard patterning. However, even in these scenarios, the monoline model had higher angle errors than did the polyline models (Perrone et al., 2015).

Polyline models are necessary for providing suitable data for verifying force inference techniques like CellFIT (Brodland et al., 2014) and for modeling complex cell shapes, such as those exhibited during invasion and engulfment. This finding suggest that the animal cell membrane must be flexible in bending in order to facilitate a wide range of reshaping and rearrangement behaviours that may be crucial to embryogenesis, several normal and disease processes, wound healing, and tissue engineering (Perrone et al., 2015). Most importantly for this thesis, the findings suggest that polyline cell edges is the appropriate model for understanding the physical mechanism that drive cells to intercalate between each other during branching morphogenesis.

6.2 Branching Morphogenesis Study

In Chapter 2, migratory epithelial cells were shown to intercalate during tube extension and bilayer resolution and localization of Ras activity, PI3K activity, and actin polymerization to epithelial protrusions were shown to precede

intercalation. However, how migratory cells drive the morphological changes remained to be mysteries. In this study, force inference analysis was used to characterize both migrating and intercalating cells within mammary organoids as having tear-drop cell shape defined by high tension in anterior protrusions and a gradient of circumferential tension which increased towards the cell posterior (Figure 21C,D). The locations of high tension correlated with F-actin accumulation revealed by the biosensor imaging and could be sites of acto-myosin mediated force generation. In addition, cells that successfully intercalated to the basal surface transitioned to non-motile columnar cells that no longer displayed high anterior protrusive tension or posterior tension gradient (Figure 21E). This finding suggests that boundary capture requires a mechanism dependent on time and space (Neumann et al., In Submission).

FE modelling was used to show that both mechanisms, independently, were sufficient at generating cell migration with an epithelial tissue (Figure 22). However, the corresponding cell shapes were not observed experimentally and the two mechanisms were considered to act in combination. This combined mechanism was also sufficient to drive intercalation; however, a time-varying mechanism was required to capture the basal surface once the intercalating cell made contact (Figure 23). Surprisingly, these cell behaviours produced disorganized growth and did not sustain elongation when incorporated into an *in silico* TEB (Figure 24A). Elongation required high basal stress, which was modeled in 2D by high basal tension in the outer-most cell layer and effective circumferential hoop stress (Figure 24B). These results were consistent with the disorganized morphology that results from disruption of basal tensions by overexpression of p190-B Rho-GAP (Vargo-Gogola, Heckman, Gunther,

Chodosh, & Rosen, 2006). Parametric analysis of the motility mechanisms revealed the relative contributions of pulling and pushing mechanisms required to achieve migration and intercalation to be similar (Figure 26C,D). A cell must extend between cells at its anterior end and release from cells at its posterior end to successfully migrate or intercalate inside a tissue. Intercalation differs from migration by the additional requirement of persistent incorporation into the basal surface (Neumann et al., In Submission).

Certainly, there are distinct ways to build epithelial tubes that differ in structure and function. For example, tube shape in the mammalian lung is regulated by mitotic spindle orientation angle (Tang, Marshall, McMahon, Metzger, & Martin, 2011), while new branches can initiate in the avian lung without proliferation (Kim, Varner, & Nelson, 2013). However, it is possible that common cell behaviours may be shared and combined in distinct ways to generate tubes with different properties. For example, computational work demonstrates that modulation of matrix elasticity or proliferation rate changes the branching pattern (Varner & Nelson, 2014).

Neither anterior protrusions nor posterior tension gradients, alone, were sufficient to elongate the *in silico* TEB because of failure to intercalate (Neumann et al., In Submission). This finding suggests the key cell behaviour in mammary branching to be radial intercalation. Intercalation is a common morphogenetic mechanism (Walck-Shannon & Hardin, 2014) and contributes to organ morphogenesis in amphibian (Szabo et al., 2016) and mammalian systems (Heller, Kumar, Grill, & Fuchs, 2014). Recent work in the Xenopus mucociliary epithelium revealed that radial intercalation increases surface area and patterns

the tissue (Sedzinski, Hannezo, Tu, Biro, & Wallingford, 2016). This study shows that intercalation both increases surface area and promotes bilayer formation in mammary gland models. In contrast, apoptosis can remove cells (Mailleux et al., 2007) but cannot elongate tubes. Recent work instead suggests that apoptosis eliminates incorrectly positioned basal phenotype cap cells from the interior of the terminal end bud (Paine et al., 2016).

7. Conclusions

Computational models provide a platform to test the plausibility of certain cellular mechanisms driving tissue-level development processes. In this study, cell migration and intercalation were shown to be sufficiently driven by varying combinations of interfacial tensions inferred from 3D imaging of *in vitro* cell shapes. Therefore, it is plausible that the Ras activity, PIP3, and F-actin enrichment observed in those locations cause migration and intercalation.

Modeling can also reveal meaningful information that may have been overlooked or not captured by physical experiment. Evidently, the model is an alternative window into the biological system and allows for exploration and experimentation in a new way. Modeling showed that a time-varying mechanism was required for intercalating cells to capture the basal surface and was critical for elongation and polarization. Modeling also showed that ordered branch elongation required high basal stress, which was shown to be present *in vitro* by pMLC staining. This suggests myoepithelial cells may play a critical role in elongation.

Iterative dialogue between traditional experiment and computational modeling critically enabled a greater understanding of the mechanical constraints on cell motility within tissues. An unusual tear-drop shape in motile cells was observed experimentally, imaging of this shape was computationally used to reveal high anterior protrusive tensions and a time-varying posterior tension gradient, and computational modeling revealed the contribution of these mechanisms to migration, intercalation, and tube elongation. Multidisciplinary studies of this

kind will enable a quantitative understanding of how cells cooperate and compete to give rise to tissues and organs.

8. Future Work

Several opportunities for future research were identified during the course of this study. First, increasing the sample size to 30 cells for predicting cell motility behaviour is needed to evaluate the use of interfacial tension ratios to predict cell motility behaviour.

Second, expanding the FE modeling to three dimensions is recommended. Although 2D FE modeling was sufficient for this study, 3D FE modeling of cell sorting has been shown to fundamentally differ from sorting in 2D FE modeling (Hutson et al., 2008). In 3D, cells have more interfaces which create more opportunities to rearrange (Hutson et al., 2008). This suggests that cells in a 3D *in silico* TEB may have more opportunities to intercalate.

Finally, further experimental work is recommended to validate the suggestion that boundary capture plays a significant role in branching morphogenesis. Experimentally quantifying the basal area and rate of intercalating cells may distinguish whether transient and permanent intercalating cells approach the basal surface with different cell shape and mechanics.

References

Affolter, M., Bellusci, S., Itoh, N., Shilo, B., Thiery, J. P., & Werb, Z. (2003). Tube or not tube: Remodeling epithelial tissues by branching morphogenesis. *Developmental Cell, 4*(1), 11-18. doi:S1534-5807(02)00410-0 [pii]

Andrew, D. J., & Ewald, A. J. (2010). Morphogenesis of epithelial tubes: Insights into tube formation, elongation, and elaboration. *Developmental Biology, 341*(1), 34-55. doi:10.1016/j.ydbio.2009.09.024 [doi]

Armstrong, P. B. (1989). Cell sorting out: The self-assembly of tissues in vitro. *Critical Reviews in Biochemistry and Molecular Biology, 24*(2), 119-149.

Armstrong, P. B., & Armstrong, M. T. (1990). An instructive role for the interstitial matrix in tissue patterning: Tissue segregation and intercellular invasion. *The Journal of Cell Biology, 110*(4), 1439-1455.

Armstrong, P. B., & Armstrong, M. T. (2000). Intercellular invasion and the organizational stability of tissues: A role for fibronectin. *Biochimica Et Biophysica Acta, 1470*(2), O9-20.

Beloussov, L. V. (1994). The interplay of active forces and passive mechanical stresses in animal morphogenesis. *Biomechanics of active movement and division*

of cells (pp. 131-180). Berlin, Heidelberg: Springer Berlin Heidelberg. doi:10.1007/978-3-642-78975-5_5"

Boal, D. H. (2012). *Mechanics of the cell* (2nd ed.). Cambridge ; New York: Cambridge University Press.

Borghi, N., Sorokina, M., Shcherbakova, O. G., Weis, W. I., Pruitt, B. L., Nelson, W. J., & Dunn, A. R. (2012). E-cadherin is under constitutive actomyosin-generated tension that is increased at cell-cell contacts upon externally applied stretch. *Proceedings of the National Academy of Sciences of the United States of America, 109*, 12568-12573. doi:10.1073/pnas.1204390109

Brodland, G. W. (2004). Computational modeling of cell sorting, tissue engulfment, and related phenomena: A review. *Applied Mechanics Review, 57*(1), 47-76.

Brodland, G. W. (1988). Highly non-linear deformation of uniformly-loaded circular plates. *International Journal of Solids and Structures, 24*(4), 351-362. doi:http://dx.doi.org/10.1016/0020-7683(88)90066-2

Brodland, G. W. (2002). The differential interfacial tension hypothesis (DITH): A comprehensive theory for the self-rearrangement of embryonic cells and tissues. *Journal of Biomechanical Engineering, 124*(2), 188-197.

Brodland, G. W. (2006). Do lamellipodia have the mechanical capacity to drive convergent extension? *The International Journal of Developmental Biology, 50*(2-3), 151-155.

Brodland, G. W., Chen, D. I., & Veldhuis, J. H. (2006). A cell-based constitutive model for embryonic epithelia and other planar aggregates of biological cells. *International Journal of Plasticity, 22*(6), 965-995.

Brodland, G. W., & Chen, H. H. (2000). The mechanics of heterotypic cell aggregates: Insights from computer simulations. *Journal of Biomechanical Engineering, 122*(4), 402-407.

Brodland, G. W., Chen, X., Lee, P., & Marsden, M. (2010). From genes to neural tube defects (NTDs): Insights from multiscale computational modeling. *HFSP Journal, 4*(3-4), 142-152. doi:10.2976/1.3338713

Brodland, G. W., Conte, V., Cranston, P. G., Veldhuis, J., Narasimhan, S., Hutson, M. S., . . . Miodownik, M. (2010). Video force microscopy reveals the

mechanics of ventral furrow invagination in drosophila. *Proceedings of the National Academy of Sciences of the United States of America, 107*(51), 22111-22116. doi:10.1073/pnas.1006591107

Brodland, G. W., & Veldhuis, J. H. (2006). Lamellipodium-driven tissue reshaping: A parametric study. *Computer Methods in Biomechanics and Biomedical Engineering, 9*(1), 17-23.

Brodland, G. W., Veldhuis, J. H., Kim, S., Perrone, M., Mashburn, D., & Hutson, M. S. (2014). CellFIT: A cellular force-inference toolkit using curvilinear cell boundaries. *PloS One, 9*(6), e99116. doi:10.1371/journal.pone.0099116; 10.1371/journal.pone.0099116

Brodland, G. W., Viens, D., & Veldhuis, J. H. (2007). A new cell-based FE model for the mechanics of embryonic epithelia. *Computer Methods in Biomechanics and Biomedical Engineering, 10*(2), 121-128.

Brugues, A., Ester, Conte, V., Veldhuis, J. H., Gupta, M., Colombelli, J., . . . Trepat, X. (2014). Forces driving epithelial wound healing. *Nat Phys, 10*(9), 683-690.

Campas, O., Mammoto, T., Hasso, S., Sperling, R. A., O'Connell, D., Bischof, A. G., . . . Ingber, D. E. (2014). Quantifying cell-generated mechanical forces within living embryonic tissues. *Nature Methods, 11*(2), 183-189. doi:10.1038/nmeth.2761; 10.1038/nmeth.2761

Capitanio, M., & Pavone, F. S. (2013). Interrogating biology with force: Single molecule high-resolution measurements with optical tweezers. *Biophysical Journal, 105*(6), 1293-1303. doi:10.1016/j.bpj.2013.08.007; 10.1016/j.bpj.2013.08.007

Chen, H. H., & Brodland, G. W. (2000). Cell-level finite element studies of viscous cells in planar aggregates. *Journal of Biomechanical Engineering, 122*(4), 394-401.

Chen, X., & Brodland, G. W. (2008). Multi-scale finite element modeling allows the mechanics of amphibian neurulation to be elucidated. *Physical Biology, 5*(1), 015003.

Chiou, K. K., Hufnagel, L., & Shraiman, B. I. (2012). Mechanical stress inference for two dimensional cell arrays. *PLoS Computational Biology, 8*(5), e1002512. doi:10.1371/journal.pcbi.1002512; 10.1371/journal.pcbi.1002512

Clausi, D. A., & Brodland, G. W. (1993). Mechanical evaluation of theories of neurulation using computer simulations. *Development, 118*, 1013-1023.

Conte, V., Muñoz, J. J., Baum, B., & Miodownik, M. (2009). Robust mechanisms of ventral furrow invagination require the combination of cellular shape changes. *Physical Biology, 6*(1), 16010.

Costantini, F., & Kopan, R. (2010). Patterning a complex organ: Branching morphogenesis and nephron segmentation in kidney development. *Developmental Cell, 18*(5), 698-712. doi:10.1016/j.devcel.2010.04.008 [doi]

Cowin, S. C., & Doty, S. B. (2006). *Tissue mechanics*. New York: Springer.

Cranston, P. G., Veldhuis, J. H., Narasimhan, S., & Brodland, G. W. (2010). Cinemechanometry (CMM): A method to determine the forces that drive morphogenetic movements from time-lapse images. *Annals of Biomedical Engineering,* doi:10.1007/s10439-010-9998-1

Davies, J. T., & Rideal, E. K. (1963). *Interfacial phenomena* (2dth ed.). New York: Academic Press.

Devreotes, P., & Horwitz, A. R. (2015). Signaling networks that regulate cell migration. *Cold Spring Harbor Perspectives in Biology, 7*(8), a005959. doi:10.1101/cshperspect.a005959 [doi]

Eaton, S., & Julicher, F. (2011). Cell flow and tissue polarity patterns. *Current Opinion in Genetics & Development, 21*(6), 747-752. doi:10.1016/j.gde.2011.08.010; 10.1016/j.gde.2011.08.010

Eisenhoffer, G. T., Loftus, P. D., Yoshigi, M., Otsuna, H., Chien, C. B., Morcos, P. A., & Rosenblatt, J. (2012). Crowding induces live cell extrusion to maintain homeostatic cell numbers in epithelia. *Nature, 484*(7395), 546-549. doi:10.1038/nature10999; 10.1038/nature10999

Ethier, C. R., & Simmons, C. A. (2007). *Introductory biomechanics : From cells to organisms*. Cambridge ; New York: Cambridge University Press.

Ewald, A. J., Brenot, A., Duong, M., Chan, B. S., & Werb, Z. (2008). Collective epithelial migration and cell rearrangements drive mammary branching morphogenesis. *Developmental Cell, 14*(4), 570-581. doi:10.1016/j.devcel.2008.03.003; 10.1016/j.devcel.2008.03.003

Ewald, A. J., Huebner, R. J., Palsdottir, H., Lee, J. K., Perez, M. J., Jorgens, D. M., . . . Auer, M. (2012). Mammary collective cell migration involves transient loss of epithelial features and individual cell migration within the epithelium. *Journal of Cell Science, 125*(Pt 11), 2638-2654. doi:10.1242/jcs.096875; 10.1242/jcs.096875

Foty, R. A., Pfleger, C. M., Forgacs, G., & Steinberg, M. S. (1996). Surface tensions of embryonic tissues predict their mutual envelopment behavior. *Devlopment, 122*, 1611-1620.

Glazier, J. A., & Graner, F. (1993). Simulation of the differential adhesion driven rearrangement of biological cells. *Physical Review E. Statistical Physics, Plasmas, Fluids, and Related Interdisciplinary Topics, 47*(3), 2128-2154.

Hanahan, D., & Weinberg, R. A. (2011). Hallmarks of cancer: The next generation. *Cell, 144*(5), 646-674. doi:10.1016/j.cell.2011.02.013; 10.1016/j.cell.2011.02.013

Harris, A. K. (1976). Is cell sorting caused by differences in the work of intercellular adhesion? A critique of the steinberg hypothesis. *Journal of Theoretical Biology, 61*(2, pp. 267-285), September. doi:10.1016/0022-5193(76)90019-9

Harris, A. K. (1994). Multicellular mechanics in the creation of anatomical structures. In Akka{\c{s} Nuri (Ed.), *Biomechanics of active movement and division of cells* (pp. 87-129). Berlin, Heidelberg: Springer Berlin Heidelberg. doi:10.1007/978-3-642-78975-5_4"

Heller, E., Kumar, K. V., Grill, S. W., & Fuchs, E. (2014). Forces generated by cell intercalation tow epidermal sheets in mammalian tissue morphogenesis. *Developmental Cell, 28*(6), 617-632. doi:10.1016/j.devcel.2014.02.011 [doi]

Hens, J. R., & Wysolmerski, J. J. (2005). Key stages of mammary gland development: Molecular mechanisms involved in the formation of the embryonic mammary gland. *Breast Cancer Research : BCR, 7*(5), 220-224. doi:bcr1306 [pii]

Hibbeler, R. C. (2011). *Statics and mechanics of materials* (3rd ed.). Boston: Prentice Hall.

Hilgenfeldt, S., Erisken, S., & Carthew, R. W. (2008). Physical modeling of cell geometric order in an epithelial tissue. *Proceedings of the National Academy of Sciences of the United States of America, 105*(3), 907-911. doi:10.1073/pnas.0711077105 [doi]

Honda, H. (1978). Description of cellular patterns by dirichlet domains: The two-dimensional case. *Journal of Theoretical Biology, 72*, 523-543.

Honda, H., Yamanaka, H., & Eguchi, G. (1986). Transformation of a polygonal cellular pattern during sexual maturation of the avian oviduct epithelium: Computer simulation. *Journal of Embryology and Experimental Morphology, 98*, 1-19.

Huebner, R. J., Lechler, T., & Ewald, A. J. (2014). Developmental stratification of the mammary epithelium occurs through symmetry-breaking vertical divisions of apically positioned luminal cells. *Development (Cambridge, England), 141*(5), 1085-1094. doi:10.1242/dev.103333; 10.1242/dev.103333

Hutson, M. S., Brodland, G. W., Yang, J., & Viens, D. (2008). Cell sorting in three dimensions: Topology, fluctuations, and fluidlike instabilities. *Physical Review Letters, 101*(14), 148105.

Hutson, M. S., Veldhuis, J. H., Ma, X., Lynch, H. E., Cranston, P. G., & Brodland, G. W. (2009). Combining laser microsurgery and finite element modeling to assess cell-level epithelial mechanics [Abstract]. *Biophysical Journal, 97*(12) 3075-3085.

Irons, B., & Shrive, N. (1983). *Finite element primer*. Chichester; New York: Ellis Horwood; Halsted Press distributor.

Ishihara, S., & Sugimura, K. (2012). Bayesian inference of force dynamics during morphogenesis. *Journal of Theoretical Biology, 313*, 201-211. doi:10.1016/j.jtbi.2012.08.017; 10.1016/j.jtbi.2012.08.017

Kasza, K. E., Vader, D., Koster, S., Wang, N., & Weitz, D. A. (2011). Magnetic twisting cytometry. *Cold Spring Harbor Protocols, 2011*(4), pdb.prot5599. doi:10.1101/pdb.prot5599

Kim, H. Y., Varner, V. D., & Nelson, C. M. (2013). Apical constriction initiates new bud formation during monopodial branching of the embryonic chicken lung. *Development (Cambridge, England), 140*(15), 3146-3155. doi:10.1242/dev.093682 [doi]

Krens, S. F., & Heisenberg, C. P. (2011). Cell sorting in development. *Current Topics in Developmental Biology, 95*, 189-213. doi:10.1016/B978-0-12-385065-2.00006-2

Krieg, M., Arboleda-Estudillo, Y., Puech, P. -., Käfer, J., Graner, F., Müller, D. J., & Heisenberg, C. -. (2008). Tensile forces govern germ-layer organization in zebrafish. *Nature Cell Biology, 10*(4), 429-436.

Lecuit, T., & Lenne, P. F. (2007). Cell surface mechanics and the control of cell shape, tissue patterns and morphogenesis. *Nature Reviews.Molecular Cell Biology, 8*(8), 633-644. doi:10.1038/nrm2222

Legant, W. R., Miller, J. S., Blakely, B. L., Cohen, D. M., Genin, G. M., & Chen, C. S. (2010). Measurement of mechanical tractions exerted by cells in three-dimensional matrices. *Nature Methods, 7*(12), 969-971. doi:10.1038/nmeth.1531

Mailleux, A. A., Overholtzer, M., Schmelzle, T., Bouillet, P., Strasser, A., & Brugge, J. S. (2007). BIM regulates apoptosis during mammary ductal morphogenesis, and its absence reveals alternative cell death mechanisms. *Developmental Cell, 12*(2), 221-234. doi:S1534-5807(06)00566-1 [pii]

Maitre, J. L., Berthoumieux, H., Krens, S. F., Salbreux, G., Julicher, F., Paluch, E., & Heisenberg, C. P. (2012). Adhesion functions in cell sorting by mechanically coupling the cortices of adhering cells. *Science (New York, N.Y.), 338*(6104), 253-256. doi:10.1126/science.1225399; 10.1126/science.1225399

Mashburn, D. N., Lynch, H. E., Ma, X., & Hutson, M. S. (2012). Enabling user-guided segmentation and tracking of surface-labeled cells in time-lapse image sets of living tissues. *Cytometry.Part A : The Journal of the International Society for Analytical Cytology, 81*(5), 409-418. doi:10.1002/cyto.a.22034; 10.1002/cyto.a.22034

Morimatsu, M., Mekhdjian, A. H., Adhikari, A. S., & Dunn, A. R. (2013). Molecular tension sensors report forces generated by single integrin molecules in living cells. *Nano Lett, 13*, 3985-3989. doi:10.1021/nl4005145

Moscona, A. (1952). Cell suspensions from organ rudiments of chick embryos. *Experimental Cell Research, 3*, 535-539.

Moscona, A. (1957). The development in vitro chimeric aggregates of dissociated embryonic chick and mouse cells. *Proceedings of the National Academy of Sciences of the United States of America, 43(1)*, 184-194.

Neumann, N. M., Perrone, M. C., Veldhuis, J. H., Zhan, H., Devreotes, P. N., Brodland, G. W., & Ewald, A. J. (In Submission). Coordination of receptor tyrosine kinase signaling and interfacial tension dynamics drive radial intercalation and tube elongation. *Developmental Cell,*

Odell, G. M., Oster, G., Alberch, P., & Burnside, B. (1981). The mechanical basis of morphogenesis: 1. epithelial folding and invagination. *Developmental Biology, 85*, 446-462.

Paine, I., Chauviere, A., Landua, J., Sreekumar, A., Cristini, V., Rosen, J., & Lewis, M. T. (2016). A geometrically-constrained mathematical model of mammary gland ductal elongation reveals novel cellular dynamics within the terminal end bud. *PLoS Computational Biology, 12*(4), e1004839. doi:10.1371/journal.pcbi.1004839 [doi]

Peng, G. E., Wilson, S. R., & Weiner, O. D. (2011). A pharmacological cocktail for arresting actin dynamics in living cells. *Molecular Biology of the Cell, 22*(21), 3986-3994. doi:10.1091/mbc.E11-04-0379 [doi]

Perrone, M. C., Veldhuis, J. H., & Brodland, G. W. (2015). Non-straight cell edges are important to invasion and engulfment as demonstrated by cell mechanics model. *Biomechanics and Modeling in Mechanobiology,* doi:10.1007/s10237-015-0697-6 [doi]

Phillips, H., & Steinberg, M. S. (1978). Embryonic tissues as elasticoviscous liquids, I: Rapid and slow shape changes in centrifuged cell aggregates. *Journal of Cell Science, 30*, 1-20.

Rappaport, R. (1977). Tensiometric studies of cytokinesis in cleaving sand dollar eggs. *The Journal of Experimental Zoology, 201*(3), 375-378. doi:10.1002/jez.1402010304

Rauzi, M., Verant, P., Lecuit, T., & Lenne, P. F. (2008). Nature and anisotropy of cortical forces orienting drosophila tissue morphogenesis. *Nature Cell Biology, 10*(12), 1401-1410. doi:10.1038/ncb1798

Ravichandran, K. S., & Lorenz, U. (2007). Engulfment of apoptotic cells: Signals for a good meal. *Nature Reviews.Immunology, 7*(12), 964-974. doi:10.1038/nri2214

Riedl, J., Crevenna, A. H., Kessenbrock, K., Yu, J. H., Neukirchen, D., Bista, M., . . . Wedlich-Soldner, R. (2008). Lifeact: A versatile marker to visualize F-actin. *Nature Methods, 5*(7), 605-607. doi:10.1038/nmeth.1220 [doi]

Sedzinski, J., Hannezo, E., Tu, F., Biro, M., & Wallingford, J. B. (2016). Emergence of an apical epithelial cell surface in vivo. *Developmental Cell, 36*(1), 24-35. doi:10.1016/j.devcel.2015.12.013 [doi]

Shakya, R., Watanabe, T., & Costantini, F. (2005). The role of GDNF/ret signaling in ureteric bud cell fate and branching morphogenesis. *Developmental Cell, 8*(1), 65-74. doi:S1534-5807(04)00406-X [pii]

Solon, J., Kaya-Copur, A., Colombelli, J., & Brunner, D. (2009). Pulsed forces timed by a ratchet-like mechanism drive directed tissue movement during dorsal closure. *Cell, 137*(7), 1331-1342. doi:10.1016/j.cell.2009.03.050

Staple, D. B., Farhadifar, R., Roper, J. C., Aigouy, B., Eaton, S., & Julicher, F. (2010). Mechanics and remodelling of cell packings in epithelia. *The European Physical Journal.E, Soft Matter, 33*(2), 117-127. doi:10.1140/epje/i2010-10677-0; 10.1140/epje/i2010-10677-0

Steinberg, M. S. (1963). Reconstruction of tissues by dissociated cells. *Science, 141*(3579), 401-408.

Steinberg, M. S. (1962). On the mechanism of tissue reconstruction by dissociated cells, I: Population kinetics differential adhesiveness, and the absence of directed migration. *Zoology, 48*, 1577-1582.

Steinberg, M. S. (1970). Does differential adhesion govern self-assembly process in histogenesis? equilibrium configurations and the emergence of a hierarchy

among populations of embryonic cells. *Journal of Experimental Zoology, 173*, 395-434.

Sternlicht, M. D. (2006). Key stages in mammary gland development: The cues that regulate ductal branching morphogenesis. *Breast Cancer Research : BCR, 8*(1), 201. doi:bcr1368 [pii]

Sternlicht, M. D., Kouros-Mehr, H., Lu, P., & Werb, Z. (2006). Hormonal and local control of mammary branching morphogenesis. *Differentiation; Research in Biological Diversity, 74*(7), 365-381. doi:S0301-4681(09)60224-3 [pii]

Szabo, A., Cobo, I., Omara, S., McLachlan, S., Keller, R., & Mayor, R. (2016). The molecular basis of radial intercalation during tissue spreading in early development. *Developmental Cell, 37*(3), 213-225. doi:10.1016/j.devcel.2016.04.008 [doi]

Tache, A., Gan, L., Deporter, D., & Pilliar, R. M. (2004). Effect of surface chemistry on the rate of osseointegration of sintered porous-surfaced ti-6Al-4V implants. *The International Journal of Oral & Maxillofacial Implants, 19*(1), 19-29.

Tambe, D. T., Croutelle, U., Trepat, X., Park, C. Y., Kim, J. H., Millet, E., . . . Fredberg, J. J. (2013). Monolayer stress microscopy: Limitations, artifacts, and accuracy of recovered intercellular stresses. *PloS One, 8*(2), e55172. doi:10.1371/journal.pone.0055172; 10.1371/journal.pone.0055172

Tang, N., Marshall, W. F., McMahon, M., Metzger, R. J., & Martin, G. R. (2011). Control of mitotic spindle angle by the RAS-regulated ERK1/2 pathway determines lung tube shape. *Science (New York, N.Y.), 333*(6040), 342-345. doi:10.1126/science.1204831 [doi]

Thomas, G., Burnham, N. A., Camesano, T. A., & Wen, Q. (2013). Measuring the mechanical properties of living cells using atomic force microscopy. *Journal of Visualized Experiments : JoVE, (76). doi*(76), 10.3791/50497. doi:10.3791/50497; 10.3791/50497

Townes, P., & Holtfreter, J. (1955). Directed movements and selective adhesion of embryonic amphibian cells. *Journal of Experimental Zoology, 128*(1, pp. 53-120), February. doi:10.1002/jez.1401280105

Vargo-Gogola, T., Heckman, B. M., Gunther, E. J., Chodosh, L. A., & Rosen, J. M. (2006). P190-B rho GTPase-activating protein overexpression disrupts ductal morphogenesis and induces hyperplastic lesions in the developing

mammary gland. *Molecular Endocrinology (Baltimore, Md.), 20*(6), 1391-1405. doi:me.2005-0426 [pii]

Varner, V. D., & Nelson, C. M. (2014). Cellular and physical mechanisms of branching morphogenesis. *Development (Cambridge, England), 141*(14), 2750-2759. doi:10.1242/dev.104794 [doi]

Veldhuis, J. H., Ehsandar, A., Maitre, J., Hiiragi, T., Cox, S., & Brodland, G. W. (2017). Inferring cellular forces from image stacks. *Philosophical Transactions B, in Press,*

Viens, D. (2006). *A 3D finite element model for the mechanics of cell-cell interactions* (PhD).

Walck-Shannon, E., & Hardin, J. (2014). Cell intercalation from top to bottom. *Nature Reviews.Molecular Cell Biology, 15*(1), 34-48. doi:10.1038/nrm3723; 10.1038/nrm3723

Wang, M. J., Artemenko, Y., Cai, W. J., Iglesias, P. A., & Devreotes, P. N. (2014). The directional response of chemotactic cells depends on a balance between cytoskeletal architecture and the external gradient. *Cell Reports, 9*(3), 1110-1121. doi:10.1016/j.celrep.2014.09.047 [doi]

Watanabe, T., & Costantini, F. (2004). Real-time analysis of ureteric bud branching morphogenesis in vitro. *Developmental Biology, 271*(1), 98-108. doi:10.1016/j.ydbio.2004.03.025 [doi]

Zienkiewicz, O. C., & Taylor, R. L. (2005). *The finite element method for solid and structural mechanics*. Oxford: Elsevier.

Glossary

Apoptosis – form of programmed cell death mediated by enzymes called caspases.

DAPI (4′,6′-diamidino-2-phenylindole) – fluorescent stain that binds to A-T rich regions in DNA.

Epithelium – layers of epithelial cells that enclose organs or line hollow organs and glands.

Extracellular Matrix (ECM) – assembly of extracellular molecules that provide structural and biochemical support to surrounding cells and tissues.

F-actin (filamentous actin) – linear polymer microfilament.

Finite Elements (FE) – numerical method for solving boundary value problems.

Green Fluorescent Protein (GFP) – protein that exhibits green fluorescence when exposed to light in the blue to ultraviolet range and used to selectively label proteins.

Intercalation – process where cells migrate between cell layers

Monoline Model – finite element model of a cell with linear edges.

Myoepithelium – layer of myoepithelial cells found in glandular tissues.

Organoid – miniaturized and simplified version of an organ.

Phosphoinositide 3-kinase (PI3K) – family of enzymes involved in cell growth, proliferation, differentiation, motility, survival, and intracellular trafficking.

Polyline Model – finite element model of a cell with connected line segments for edges.

Ras – family of proteins involved in cell signalling transduction.

Root Mean Square (RMS) – a measure mathematically defined as the square root of the arithmetic mean of the squares of a set of numbers.

Terminal End Bud (TEB) – the tip of an epithelial branch in morphogenesis.

Watershed Algorithm – image processing transformation for segmenting an image into regions.